# Exploring the Peierls-Distorted Vanadium Sulphide as A Rechargeable Mg-Ion Cathode

Sunita Dey,[a] Jeongjae Lee,[a] Sylvia Britto,[a,b] Joshua M. Stratford,[a] Giannantonio Cibin,[b] Evan N. Keyzer,[a] Simon J. Cassidy,[c] Mahmoud Elgaml [c], Matthew T. Dunstan,[a] and Clare P. Grey[*, a]

[a]Department of Chemistry, University of Cambridge, Lensfield Road, Cambridge, CB2 1EW, UK
[b]Diamond Light Source, Harwell Science and Innovation Campus, Didcot, UK
[c]Department of Chemistry, University of Oxford, South Parks Road, Oxford, OX1 3QR, UK
*cpg27@cam.ac.uk

Fax: (+44)1223336362; Tel: (+44)1223336509

## Abstract

For magnesium ion batteries (MIB) to be used commercially, new cathodes must be developed that show stable reversible Mg intercalation. $VS_4$ is one such promising material, with vanadium and disulphide anions $[S_2]^{2-}$ forming one dimensional linear chains, with a large interlayer spacing (5.83 Å) enabling Mg insertion. However, little is known about the details of the redox processes and structural transformations that occur upon Mg intercalation and deintercalation of $VS_4$. Here we use a suite of local structure characterization methods including XPS, V and S X-ray Absorption Near Edge Spectroscopy and $^{51}V$ Hahn-Echo and Magic Angle Turning with Phase Adjusted Sideband Separation NMR to elucidate the complex electrochemical reaction pathways. We show that the reaction proceeds via internal electron transfer from $V^{4+}$ to $[S_2]^2$, resulting in the simultaneous and coupled oxidation of $V^{4+}$ to $V^{5+}$ and reduction of $[S_2]^{2-}$ to $S^{2-}$. We report the formation of a previously unknown intermediate in the Mg-V-S compositional space, $Mg_3V_2S_8$, which is made of $[VS_4]^{3-}$ tetrahedral units and identified using an evolutionary structure predicting algorithm and verified experimentally via X-ray Pair Distribution Function analysis. Subsequent magnesiation gives rise to the reduction of $V^{5+}$ towards $V^{4+}$. Further magnesiation sees conversion to MgS plus V metal; this reaction potential is close to the conversion potential of $VS_4$ to $Mg_3V_2S_8$, leading to competing reaction pathways. Demagnesiation results in the reformation of the $V^{5+}$, $S^{2-}$ containing intermediate instead of $VS_4$. This work showcases the possibility of developing a family of transition metal polychalcogenides functioning via anionic as well as combined cationic-anionic redox processes, as a potential way of achieving higher capacities for MIBs.

## Introduction

Research in Mg ion batteries (MIB) has increased considerably in recent years with the aim of improving energy density, safety and reducing cost. Mg metal is highly abundant, offering a high theoretical volumetric capacity of 3833 mAh/cm when used as a anode, and its use avoids the risk of thermal runaway since, unlike lithium metal, it is not prone to dendrite formation.[1-3] Progress is, however, limited by cathode development in part due to the poor mobility of the highly charged $Mg^{2+}$ ions in the cathode electrode materials.[1] The higher polarizability of sulphur promotes much better bulk $Mg^{2+}$ ion diffusion in transition metal (TM) sulphides compared to oxides,[4-8] with cathodes such as the $Mo_6S_8$ Chevrel phase achieving a stable capacity of 70 mAh/g over 2000 cycles.[9] While sulphides typically show low insertion potentials, high energy densities can still be achieved by increasing the capacity. One approach is to use conversion electrodes such as CuS, which offer a much higher specific capacity, in spite of poor kinetics, the redox active material breaking down to Cu metal and MgS through non-topotactic structural changes.[10]

High specific capacity can also be achieved by exploiting electrode materials that operate through combined cationic-anionic redox transformation or exclusively through anionic processes, e.g., in the lithium – sulphur battery.[11] Previous studies of transition metal sulphides containing discrete $[S_2]^{2-}$ bonds (e.g. $FeS_2$, $TiS_3$, $VS_4$) have found that both the cations and anions are also redox active during Li ion insertion-deinsertion.[11-13] In particular, $VS_4$ was shown to react with Li and Na stably over 50 cycles with capacities of 727 mAh/g and 250 mAh/g respectively,[14-16] with the electrochemical process leading to the formation of amorphous products. In addition, the extensive overlap of the S(sp) bands with metal(d) orbitals means that the reduction/oxidation no longer occurs exclusively involves the metals, enabling complex reaction pathways. Therefore, the challenge remains to propose the correct mechanism in order to improve the performance. Subsequently Britto *et al.*[17] found that Li intercalation in $VS_4$ was accompanied by multiple redox processes involving an insertion stage followed by conversion.

$VS_4$ crystallizes in a monoclinic, I2/c, space group,[18](Figure 1), with all S present as dimerized persulphide units with formal charge of -1, octahedrally coordinated to $V^{4+}$ and arranged in a linear chain structure. This linear chain extends along the c axis and is comprised of alternating V-V distances of 3.2 and 2.8 Å, with an interchain spacing of 5.83 Å, making it a promising candidate for $Mg^{2+}$ insertion. In a recent report by Wang *et al.*,[19] $VS_4$ displayed highly reversible (de)insertion of Mg ions, with an uptake of 0.84 mol Mg per mol of $VS_4$ during the first discharge (corresponding to a capacity of ~250 mAh/g) at a rate of C/12 and a capacity of 0.5 mol Mg (~177 mAh/g) at higher cycle numbers. *Ex situ* X-ray diffraction (XRD) experiments in the same study[19] did not observe any changes in the XRD pattern of $VS_4$ during Mg (de)insertion, with further structural analysis prevented by the poor resolution of the Bragg peaks due to the poor crystallinity of the disordered/amorphous phase formed after electrochemical cycling. X-ray Photoelectron Spectroscopy (XPS) showed the surface oxidation of $V^{4+}$ to $V^{5+}$ and reduction of $[S_2]^{2-}$ to $S^{2-}$ by the end of discharge,[19] but further details concerning of surface and structural changes at intermediate voltages are needed. Upon charging, reformation of $VS_4$ was inferred, with the change in intensity and shift in energy of the broad S2p photoelectron peak assigned to partial oxidation of $[S_2]^{2-}$. However, XPS does not show any evidence of reduction of $V^{5+}$ to $V^{4+}$. The observed Raman signals are fairly broad and too weak to confirm the reappearance of $[S_2]^{2-}$ or the formation of any other intermediate species on

2

(dis)charging. These observations raise several questions regarding the structural transformations occurring on reaction with $Mg^{2+}$, whether conversion occurs, and whether $VS_4$ reforms on charging, as well as the actual structure of any intermediate phases.
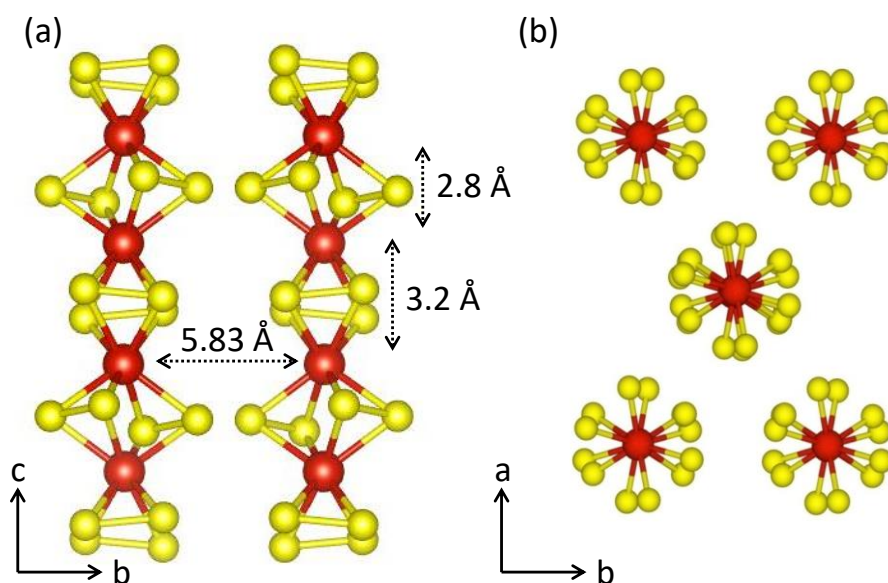


**Figure 1.** *(a) $VS_4$ structure projected down the a-axis. Red and yellow balls are vanadium and sulphur, respectively; the interchain spacing is 5.8 Å. The Peierls distorted structure contains V-V distances of 3.2 and 2.8 Å. (b) Side view of $VS_4$ showing the arrangement of chains down the c axis.*

In this paper, we revisit the magnesium electrochemistry of $VS_4$, utilising local structural characterization tools including X-ray photoelectron spectroscopy (XPS), X-ray absorption near-edge spectroscopy (XANES), solid state nuclear magnetic resonance spectroscopy (ssNMR) and X-ray pair distribution function (XPDF) analysis to track the structures formed upon charge and discharge. Surface sensitive XPS, along with S and V K edge XANES, is used to follow the simultaneous changes in redox state of S and V during the initial electrochemical cycle, and together with [51]V magic-angle spinning (MAS) ssNMR, to identify distinct chemical environments corresponding to local structural changes along the reaction pathway along with a new intermediate phase with short range order.

The Mg-$VS_4$ compositional space has previously been explored up to 0.875 insertion of mol $Mg^{2+}$ ions/mol of $VS_4$ by Wang *et al.*[19], with the evaluation of energetically favourable structures carried out using density functional theory (DFT). However, structures within the general [$M^{2+}$, $V^{5+}$, $S^{2-}$] phase space (M is IIA elements of periodic table) have not been previously explored, including the [$Mg^{2+}$, $V^{5+}$, $S^{2-}$] phase diagram of interest. To this end we employed an evolutionary structure prediction method aimed at identifying potential structural candidates for the intermediate. This method of *ab initio* crystal structure prediction produces many generations of structures, the approach effectively mimicing natural selection by identifying the most stable structures by a "survival of the fittest" methodology. It has previously been successfully used to identify functional materials with novel structures, including superhard materials, battery electrodes, and thermoelectrics.[20] Combining this theoretical approach with XPDF experiments, we report a new

phase in the Mg-V-S compositional space, $Mg_3V_2S_8$, which appears as an intermediate phase during the electrochemical process.

This study establishes $VS_4$ as a viable MIB cathode by elucidating its electrochemical reaction pathway and structural evolution through combined theoretical and experimental efforts. For the first time in a Mg ion battery electrode, conclusive evidence for a metastable intermediate formed through a local internal electron transfer mediated by cation anion redox has been shown, providing valuable insights towards designing stable, reversible Mg ion cathodes in the future. To the best of our knowledge, the $Mg_3V_2S_8$ phase has never before been synthesized and is a good example of how electrochemical processes can lead to the formation of unusual metastable phases.

## Results

### Electrochemistry.

The electrochemical Mg intercalation-deintercalation of $VS_4$ was carried out at various C rates between 1.8-0.3 V (Figure 2 and S1, see materials and method for more details). The first discharge curve, performed at a rate of C/50, shows a total uptake of 0.83 Mg per formula unit (f.u.) of $VS_4$ (corresponding to a specific capacity ~250 mAh/g). An initial downward slope is seen, then a flat extended plateau at around 1.1 V, which is followed by a gradual sloping behaviour until reaching the cut-off voltage of 0.3 V. Nearly half of the capacity is associated with the 1.1 V plateau. The charging profile displays a sharp rise in voltage until reaching a plateau at 1.4 V. 0.17 Mg/f.u. of $VS_4$ was deintercalated, which is half of that intercalated during the 1.1 V discharge process. Charging ends with a gradual sloping profile, with a total of 0.57 Mg/f.u. of $VS_4$ deintercalated.
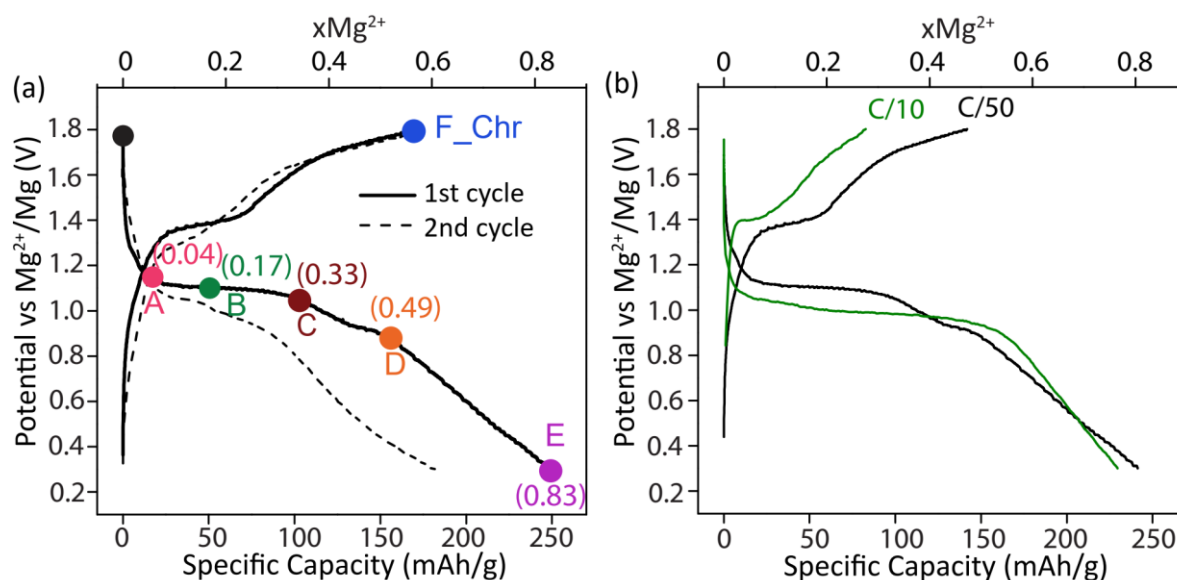


***Figure 2.*** *Galvanostatic charge-discharge curve of $VS_4$ cycled at a rate of C/50 (a) for the first two cycles and (b) as compared with the curve obtained with a cycle rate of C/10. The cathode has been stopped at various states of discharge (points A-E) and charge (point F) during the 1st cycle (rate of C/50). The moles of reacted Mg/f.u. of $VS_4$ are shown in parentheses.*

4

The second cycle shows a reversible capacity of 0.57 mol Mg per mole of VS$_4$, with a shorter plateau (Figure 2a). Cycling at a rate of C/10 or C/50 gives approximately the same capacity during the first discharge, while upon charging, the capacity decreases more for the higher C/10 rate and a significant increase in voltage hysteresis is seen (Figure 2b). Nonetheless VS$_4$ shows reversible Mg intercalation-deintercalation even at higher rates (Figure S1), galvanostatic cycling at rates of C/10 and C/3 giving specific capacities of 100 and 80 respectively for 20 cycles, with a capacity retention of 40 mAh/g over 200 cycles at 2C.

## Reaction pathways and local structure evaluation

### *X-ray photoelectron spectroscopy.*

XPS analyses were carried out on VS$_4$ discharged to various potentials (samples A-E) and charged back to 1.8 V (sample F) so as to monitor the change in oxidation state and chemical composition of sulphur (Figure 3). The S2p spectrum of VS$_4$ has two signature peaks at binding energies of 164.1 (S 2p$_{1/2}$) and 162.9 eV (S 2p$_{3/2}$) corresponding to the S$_2^{2-}$ dimer. All the spectra were fitted by assuming that the spin-orbit splitting energy and intensity ratio between S 2p$_{3/2}$ and S 2p$_{1/2}$ peak is 1.16 eV[21] and 0.5, respectively. At the beginning of discharge, the S2p spectrum can be deconvoluted mainly with two pairs of peaks, with an overall decrease in binding energy, indicating the reduction of the S$_2^{2-}$ dimers (Samples A and B). The two S 2p$_{3/2}$ binding energies of these peaks are located at 162.4eV and 161.7eV, corresponding to S$^{2-x}$ (0≤x≤1) and S$^{2-}$ ions respectively. The S$^{2-x}$ peak is broad (FWHM= 1.78 eV), indicative of a wide distribution of S redox states and V-S bond distances. Upon further discharge to 1.06V and 0.9 V, the broad S$^{2-x}$ peaks gradually disappear while the position of the S$^{2-}$ peaks remain constant while increasing in intensity. At the end of discharge, only the peak corresponding to S$^{2-}$ is evident indicating the complete reduction of the S$^{2-x}$ ions. The metal sulphide (S 2p$_{3/2}$) binding energy is reported to be around 161.5 eV, close to the value observed here of 161.7eV, consistent with the formation of MgS at the end of discharge.[21] On charging to 1.8 V (sample F), the S$^{2-}$ peak intensity reduces and the broad peak assigned to S$^{2-x}$ reappears, indicating that sulphur is redox active during (de)intercalation of Mg ions. The S 2p$_{3/2}$ peak of S$^{2-x}$ is centred at 162.4 eV, negatively shifted by 0.5 eV compared to the corresponding S 2p$_{3/2}$ peak of VS$_4$. As the S$^{2-x}$ peaks are very broad, it is not possible to determine whether VS$_4$ is reforming at the end of charge. However, the spectrum on charge resembles that of samples A and B, indicating a partially reversible redox process in this voltage range.
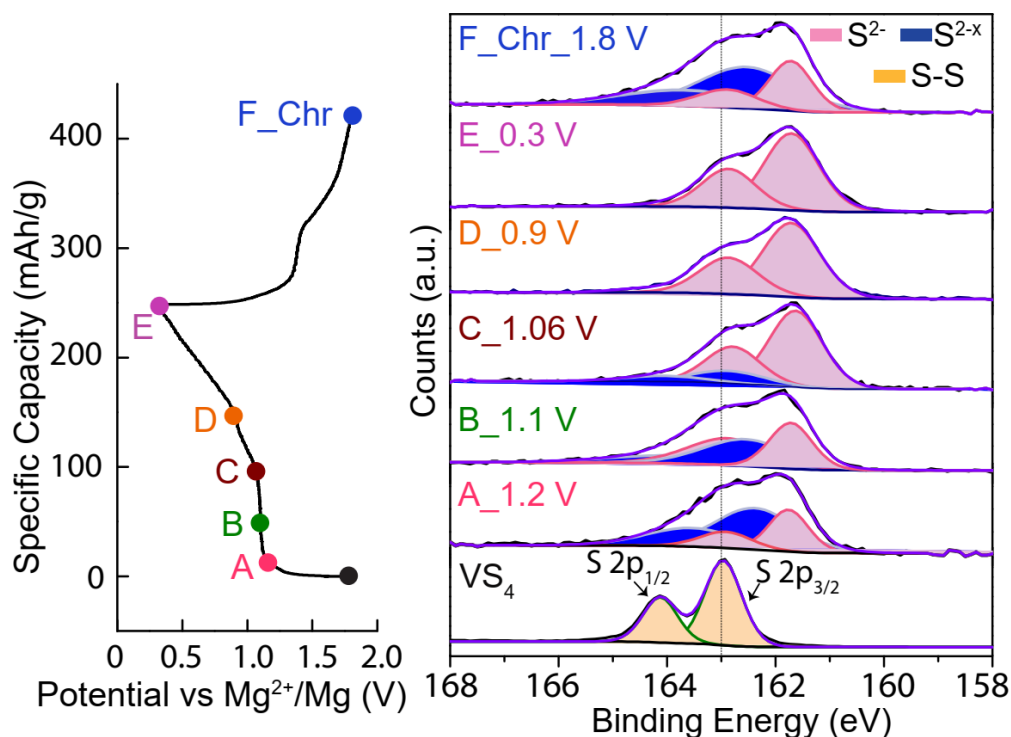
**Figure 3.** *S2p photoelectron spectra of VS$_4$ at different states of discharge and charge. The recorded spectra and resultant fit are marked in black and violet respectively.*

## S and V K-Edge XANES Spectroscopy.

Since XPS results only report on surface and sub-surface environments, XANES of the S and V K edges was performed to elucidate the oxidation state changes and identify any charge transfer between the vanadium and sulphur ions in the bulk as a function of (de)magnesiation (Figures 4 and S2). The normalized absorption spectra and their derivatives are plotted in Figure 4, while the subsequent changes in V and S K edges for selected states of charge are shown side by side in Figure S2, more clearly showing the subtle changes in the peaks as a function of discharge and charge.

Electronic excitations from the S1s to the S3p/V3d antibonding states give rise to S K edge features in vanadium sulphides. The changes in S edge peak and intensity are sensitive to two factors: (i) the oxidation state and ionicity of S and (ii) the covalency of V-S bonds. Accordingly, the relative peak shift is not only a function of S oxidation state but also of the oxidation state of the V ion. Consistent with this, the S K edge XANES spectra of the model compounds studied here (K$_3$VS$_4$, VS$_2$, LiVS$_2$, S and MgS, Figure S3a, see Methods for their synthesis details) show a decrease in S edge peak from 2469.8 to 2468.7 eV with increasing V oxidation state, from +3 (LiVS$_2$) to +4 (VS$_2$) and to +5 (K$_3$VS$_4$). The higher the V oxidation state, the more stabilized the S3p/V3d hybridized antibonding orbitals become, and as a result the S edge peak shifts to lower energy. However, the XANES spectrum of the more ionic material MgS, contains a peak at much higher energy (~ 2473 eV).
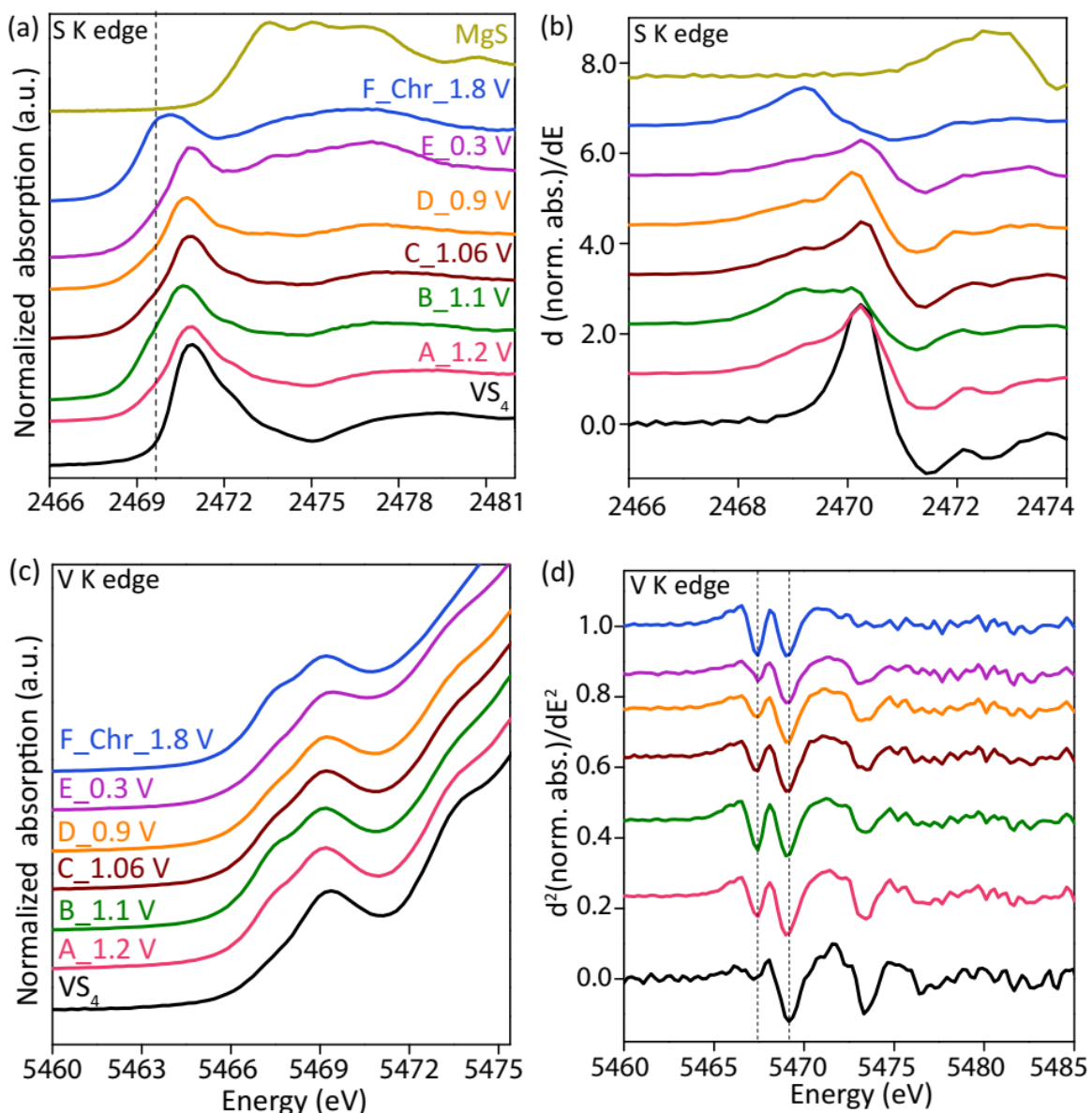
**Figure 4.** *(a, b) S and (c, d) V Kedge XANES spectra of VS₄ at different states of discharge and charge. (a) Normalized absorption and corresponding (b) first derivative S K edge XANES spectra. The spectrum of MgS is shown in dark yellow as a reference. (c) Normalized absorption and (d) second derivative V spectra (vertically offset by 1.1) are shown focusing on the V pre edge and beginning of the K edge. The extended energy range for the V XANES spectra along with more model compounds are shown in supporting figures S2 – S6.*

VS₄, with S-S dimers (-1 formal charge) shows a S edge peak at 2470.2 eV. On discharging to 1.2 V, an additional new peak emerges at lower energy (~2469.2 eV), which grows in intensity on discharging to 1.1 V (Figures 4a and b); the peak is assigned to a new intermediate and to the reduction of $S_2^{2-}$ to $S^2$. VS₄ also shows a V pre edge peak at 5469.2 eV.[22] Upon discharging to 1.2 V, a new pre edge peak emerges at ~5467.4 eV, which grows in intensity on further discharge to 1.1 V (Figures 4c and d). The V pre edge feature arises from dipole forbidden 1s to 3d electronic excitations and can be used as a qualitative signature of symmetry change.[22, 23] Lowering the

structural symmetry from octahedral ($O_h$) to tetrahedral ($T_d$) allow this 1s to 3d absorption, tetrahedral environments giving rise to strong V pre edge feature as demonstrated in Figure S3b with V K edge XANES of the model compounds {($LiVS_2$, $O_h$), ($VS_2$, $O_h$) and ($K_3VS_4$, $T_d$) [24]}, where the $T_d$ $VS_4$ unit in $K_3VS_4$ gives rise to an intense pre edge peak in $K_3VS_4$ (as previously reported for $Cu_3VS_4$[22, 25]). The pre edge energy of the new peak seen here closely matches that of $K_3VS_4$ (~5467.4eV, Figure S3b), and is consistent with the oxidation of $V^{4+}$ to $V^{5+}$ and concomitant reduction of $S_2^{2-}$ to $S^{2-}$ leading to this new phase.

On discharging further to 1.06 V (Sample C), the S K edge energy increases, albeit to a smaller extent (Figure S2b). An accompanying drop in intensity of the $V^{5+}$ pre edge peak is observed (Figure S2f), suggesting an increase in symmetry around the V atom. This change in V symmetry is tentatively assigned to the reduction of $V^{5+}$ to $V^{4+}$. This decrease in V oxidation state is expected to have profound effect on metal ligand covalency and as a result increases the S3p/V3d antibonding energy, which in turn is responsible for the small increase seen in S K edge energy. Similar shifts continue upon further discharge to 0.9 V. The $V^{5+}/V^{4+}$ pre edge area ratio increases from 0.2 to 0.61 after discharging to 1.1 V (Table S1, here, we restrict ourselves to using this integrated area under the V XANES peak as a qualitative measure of oxidation state). However, on discharge to 0.9 V the $V^{5+}/V^{4+}$ area ratio decreases gradually to 0.41, further indicating $V^{5+}$ is reduced during these processes.

Upon discharge to 0.3 V, the intensity of the S edge peak decreases significantly, while a broad peak between 2472-2481 eV suddenly appears (sample E, pink curve, Figures 4a and S2c), which is ascribed to the formation of MgS. The S K edge of the MgS starts at ~2472 eV and the characteristic absorption energy peaks of MgS are quite prominent at sample E (Figure S4a). In addition, a S K edge absorption at around 2470 and 2469 eV is observed, arising from unconverted $VS_4$ and the remaining intermediate resulting from previous discharge processes respectively (Figure S5). Interestingly, V XANES shows a change in slope of the curve associated with a decrease in V K edge energy (sample E, see Figure S2g), presumably due to the formation of V metal. The edge energy of sample E is different than that of commercially obtained V metal (Figure S4b),[26] which could be due (in part) to the incomplete conversion of $VS_4$ and the formation of nanoscale V metal crystallizing in metastable crystal structure (a proposal investigated with the NMR and PDF experiments described below). Similar observations have been seen in the Li/$FeS_2$ system, where the Fe XAS energy of disordered Fe nanoparticles formed at the end of first discharge differed from that of Fe bulk metal.[27]

On charging to 1.8 V (sample F, blue curve, Figures 4a and b) the S edge energy decreases to 2469.3 eV. The V pre edge energy also reappears to ~5467.4 eV (Figures 4c and d) and the V edge energy increases (see Figure S2h); the $V^{5+}/V^{4+}$ ratio increases to 0.66 (Table S1), which confirm the formation of a [$V^{5+}$, $S^{2-}$] like phase upon demagnesiation.

To extract qualitative information of the MgS content at the end of discharge (E) and charge (F) we carried out target transformation-Principal component analyses (PCA) of the S XANES data (for more calculation details see Figure S7). The residue plot improved drastically when a component corresponding to MgS was included in the PCA for sample E, confirming its formation at the end of

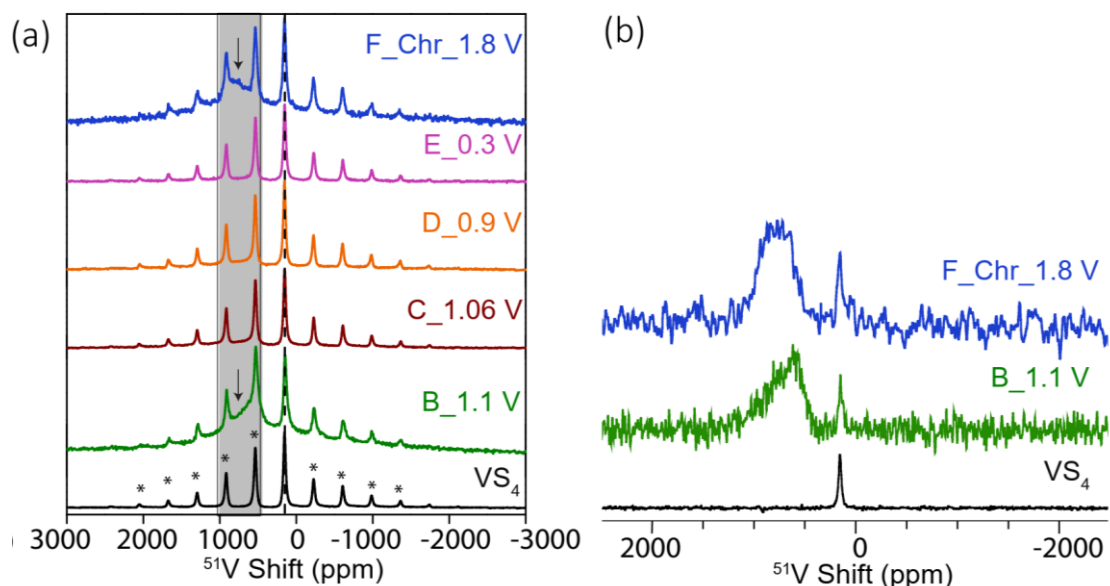discharge; this effect is much smaller for sample F, indicating that MgS is removed during demagnesiation.



**Figure 5.** *(a)  Hahn echo $^{51}$V NMR spectra of VS$_4$ at various states of discharge and charge. Spectra are acquired at 11.7 T at a MAS rate of 50 KHz. The isotropic shift of VS$_4$ is at 164 ppm, marked by vertical dashed line. Asterisks denote spinning sidebands. The grey shaded area highlights the appearance of an additional broad resonance in sample B (1.1 V discharge) and sample F (1.8 V charge). Spectra recorded at a MAS of 25 kHz are shown in supporting figure S8. (b) MATPASS NMR spectra of VS$_4$, sample B and F.*

*Hahn Echo and MATPASS $^{51}$V solid state NMR.*

 $^{51}$V NMR was carried out in order to probe the changes in local structure and V redox associated with local VS$_4$ structural motifs upon (de)magnesiation. VS$_4$ shows a characteristic isotropic shift at 163 ppm consistent with the paired V$^{4+}$ d$^1$ electrons in the Peierls distorted structure and in agreement with the previous report (Figure 5a).[17] The intensity of the VS$_4$ resonance (~163 ppm) decreases gradually on magnesiation (Figure S8b). The decrease is accompanied by the growing intensity of a peak around 5660 ppm, more evidently from 1.06 V onwards (Figure S8c), assigned to V metal in its face centred cubic polymorph V(fcc). The thermodynamic phase of V metal adopts a body centred cubic structure, with a chemical shift around 5230 ppm.[17, 28] The formation of metastable V(fcc) is also supported by PDF measurements as discussed in the following section.

Hahn Echo $^{51}$V NMR experiments at a faster MAS speed of 50 kHz performed to increase the effective spectral distance between sidebands (Figure 5a) showed that upon discharging to 1.1 V an additional broad signal becomes visible (highlighted by the grey shaded area) in addition to the characteristic peaks of VS$_4$. On discharging further, this extra resonance disappears, and emerges again only upon charging to 1.8 V (sample F, blue spectra). These features were not observed while spinning the samples at lower speed of 25 kHz (Figure S8a). However, even at the faster MAS rate, this new peak of interest is obscured by the spinning sidebands.

9

We therefore utilized a method for efficient 'sideband separation', namely, projection magic angle turning and phase-adjusted sideband separation (MATPASS). The MATPASS experiment has been employed earlier for moderately quadrupolar nuclei in paramagnetic environments.[29, 30] By applying this technique to $VS_4$ discharged to 1.1 V (green spectra) and charged to 1.8 V (blue spectra), we are able to clearly observe a broad feature between 300-1300 ppm, in addition to the characteristic $VS_4$ peak at 164 ppm (Figure 5b). We ascribe this new resonance (~300-1300 ppm) to the formation of diamagnetic $V^{5+}$ ions consistent with the $^{51}V$ NMR shift of $K_3VS_4$ (1375 ppm; Figure S9); the shift of the thiovanadate ion ($VS_4^{3-}$) in solution is reported to be in the same range (1380-1400 ppm).[31, 32]

Upon demagnesiation (sample F) the intensity of the 163 ppm resonance remains similar to that of 0.3 V discharged $VS_4$ (sample E), while the V(fcc) peak decreases in intensity (Figures S8d). These results indicate that upon demagnesiation $VS_4$ does not reform, although nearly half of the V(fcc) has been consumed in the oxidation process.

*X-ray Pair Distribution Function Analysis (XPDF).*

To obtain more detailed structural information for the intermediates formed during electrochemical cycling of $VS_4$, X-ray PDF total scattering data for four selected samples were collected. The XPDF pattern of pristine $VS_4$ shows the correlations due to S-S dimers and V-S distances at 2.0 Å and 2.4 Å respectively (Figure 6, Table S2). On discharging to 1.1 V, an intense, new correlation appears at 2.28 Å with a shoulder at 1.96 Å, corresponding to the formation of an intermediate phase (Figure 6, sample B). High *r* correlations (10-30 Å) at this state of charge resemble those of $VS_4$ (Figure S10), implying the presence of two phases: one with short-range order and the other crystalline $VS_4$. Due to the strong X-ray scattering power of V, the XPDF peaks are likely dominated by contributions from V-S and V-V correlations. The major changes appearing at r ≤10 Å are consistent with the formation of highly disordered vanadium environments, while the sharpness of 2.28 Å peak compared to the other peaks indicates that these local V units are well defined.

At the end of discharge (Sample E) an entirely new set of peak appears, matching those of metastable V(fcc) (space group Fm-3m, a= 3.819 Å). This phase dominates the XPDF intensity due to the strong V-V X-ray scattering factors. The data can be modelled with the known V(fcc) structure [28] with *a* = 3.616 Å and particle size ≥ 50 Å.
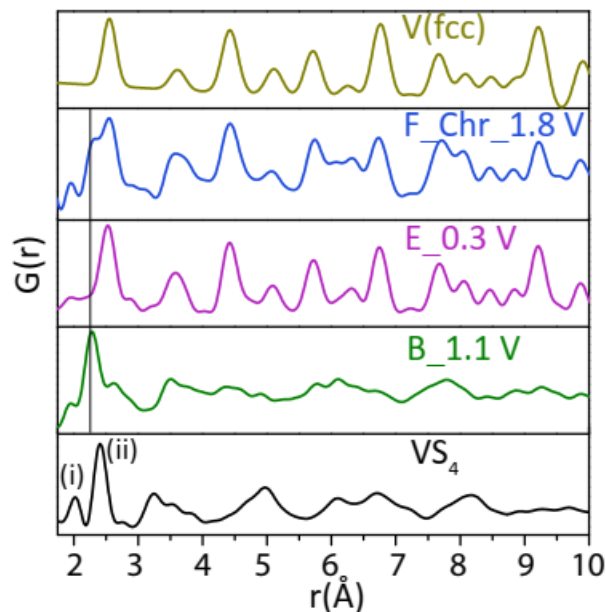
**Figure 6.** *Pair distribution function data of $VS_4$ during three different states of discharge and charge. The PDF pattern of V(fcc) is shown on top as a reference. S-S dimer and V-S distances in $VS_4$ are denoted by (i) and (ii) respectively while the black line is given for visual reference to follow the changes in V-S correlations during cycling.*

*Structural determination of the intermediate phase by theory and experiment.*

Collectively our results point to the existence of a new intermediate upon discharge to 1.1 V forming alongside the V(fcc) phase at higher states of discharge. The Mg-V-S phase diagram does not contain any known phases and we are not aware of any detailed theoretical studies of this phase diagram. Hence, we consulted the Materials Project[33] and systematically examined predicted phases with formation energies consistent with a theoretical reaction potential of 1.1-1.3 V (see Table S3). XPDF patterns were generated for all the identified phases: $MgVS_3$, $Mg(VS_2)_4$, $Mg(VS_2)_2$ and $MgV_2S_5$[33]. However, none of the simulated patterns provided a good match to our experimental XPDF data. We, therefore, turned to theoretical structural solution methods, to identify new potential candidates, making use of the $V^{5+}$ and $S^{2-}$ oxidation states determined from the XPS and XANES data. Starting with $VS_4$, magnesiation to produce a compound containing $V^{5+}$ and $S^{2-}$ oxidation states should correspond to a composition $Mg_3V_2S_8$; however, no such compound has been reported to date.

Next an *ab initio* structure generation method approach was employed with uses the USPEX (Universal Structure Predictor: Evolutionary Xtallography) algorithm[34-36], which seeks to predict stable structures solely from compositional information. An initial set, or generation, of structures is created by randomly placing atoms (obeying stoichiometry constraints) in an arbitrarily chosen space group, which are then relaxed using DFT. The lowest energy ($\Delta H_f$) structures are taken and supplemented with more random structures to produce the next generation, the structures of which are again relaxed, and so on. The lowest energy structure with composition $Mg_3V_2S_8$ was found using a total of 64 generations with 50 structures in each generation. The structure is monoclinic with lattice parameters of *a* = 7.60 Å, *b* = 13.35 Å, *c* = 12.38 Å and β = 106.68°, with a unit cell volume of

11

1204.01 Å$^3$ (Figure 7, Table S4). The structure contains two chemically equivalent vanadium sites and three Mg environments of equal occupation, two of which adopt an equivalent 6-fold coordination and one that is 5-coordinate. It is best described as a variation of the AB$_2$ layered structure with two modifications: (i) alternating layers consisting of octahedrally coordinated Mg$^{2+}$ and tetrahedrally coordinated V$^{5+}$ and (ii) honeycomb-ordered Mg vacancies within the Mg layers (Figure 7). Thus, the structural formula could alternatively be rewritten as $[(Mg_{3/2}\square_{1/2})S_4]^{5-} V_{1/2}^{5+}$ to more clearly show the layered nature of this compound. The presence of vacancies within the Mg layer and voids within the V layer generates open channels along all three lattice directions, which could potentially enable fast ionic conductivity. Our DFT calculations predict the formation enthalpy (ΔH$_f$) of Mg$_3$V$_2$S$_8$ to be -1172.3 kJ/mol per formula unit; this phase is therefore expected to be thermodynamically stable with respect to the elemental mixtures. It is also expected to be dynamically stable given the absence of negative frequency modes in the phonon dispersion curve (Figure S11), indicating that there are no phonon modes which could lead to a symmetry-lowering phase transition. However, considering the unsuccessful attempts to synthesize this compound which always results in the formation of V$_5$S$_8$, S and MgS, Mg$_3$V$_2$S$_8$ appears to be metastable with respect to other Mg-V-S phases in the phase diagram.
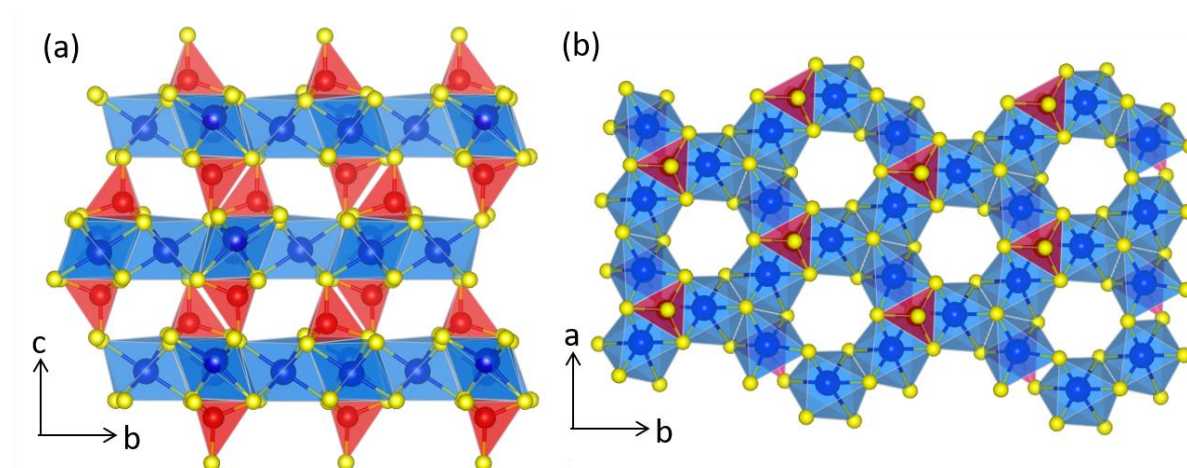


**Figure 7.** *USPEX-generated* Mg$_3$V$_2$S$_8$ structure viewed down the (a) *a* and (b) *c* axis. *V, S and Mg atoms are shown in red, yellow and blue, respectively.*

Least squares refinement of this novel Mg$_3$V$_2$S$_8$ structure against experimental XPDF data for sample B (1.1 V) shows a good fit out to a range of 10 Å (Rw= 23.4%, Figure 8a, left graph, Table S5). Fitting to sample E (0.3 V) required a secondary V(fcc) phase in a two-phase refinement (Figure 8a, middle graph, Table S5), with a good fit against the data for the two phases (Rw =19.2%). The phase fraction of V metal is 6.1% at the end of discharge, derived from the PDF scale factor. The peaks due to V(fcc) interatomic distances weaken in intensity upon charge while those due to Mg$_3$V$_2$S$_8$ increased, confirmed by a two phase refinement on sample F (Figure 8a, right graph, Table S5), leading to a phase fraction for the V metal of 1.2 % at the end of charge.

Extracted PDF correlations arising from the Mg$_3$V$_2$S$_8$ based intermediates are presented in Figure 8b. In sample B (composition Mg$_{0.17}$VS$_4$ based on electrochemistry data), correlations at 2.28 Å and 2.62 Å correspond to V-S bond lengths matching vanadium sulphide T$_d$ units in the Mg$_3$V$_2$S$_8$ structure. By

the end of discharge (sample E, composition $Mg_{0.83}VS_4$), these correlations lengthen to 2.44 Å and 2.66 Å respectively, the increase in average V-S bond distances arising from partial reduction of $V^{5+}$. This finding supports the XANES results during the 1.06-0.90 V plateau (see Figure S2b and f), where the intensity of the V pre-edge peak decreases on going from 1.1 V to 1.06 V accompanied by a small increase in S edge position. Upon charging, these shifts are reversed, with correlations at 2.35 Å and 2.61 Å being observed, respectively (sample F, composition $Mg_{0.25}VS_4$), consistent with the partial reformation of the $Mg_3V_2S_8$ intermediate. In samples B and F an additional peak at 1.94-1.96 Å is seen which corresponds to Mg-S correlations that are visible due to the absence of V-S/S-S peaks. The width of the V-S peak indicates the breadth of distribution of V-S bond lengths within vanadium sulphide $T_d$, with the wider peak of sample F indicating a greater distribution of V-S distances in agreement with the broad $^{51}V$ resonances seen in the MATPASS NMR spectra. The intermediate phase becomes more crystalline in samples E and F, its corresponding peaks growing in intensity out to 20 Å (Figure 8a).
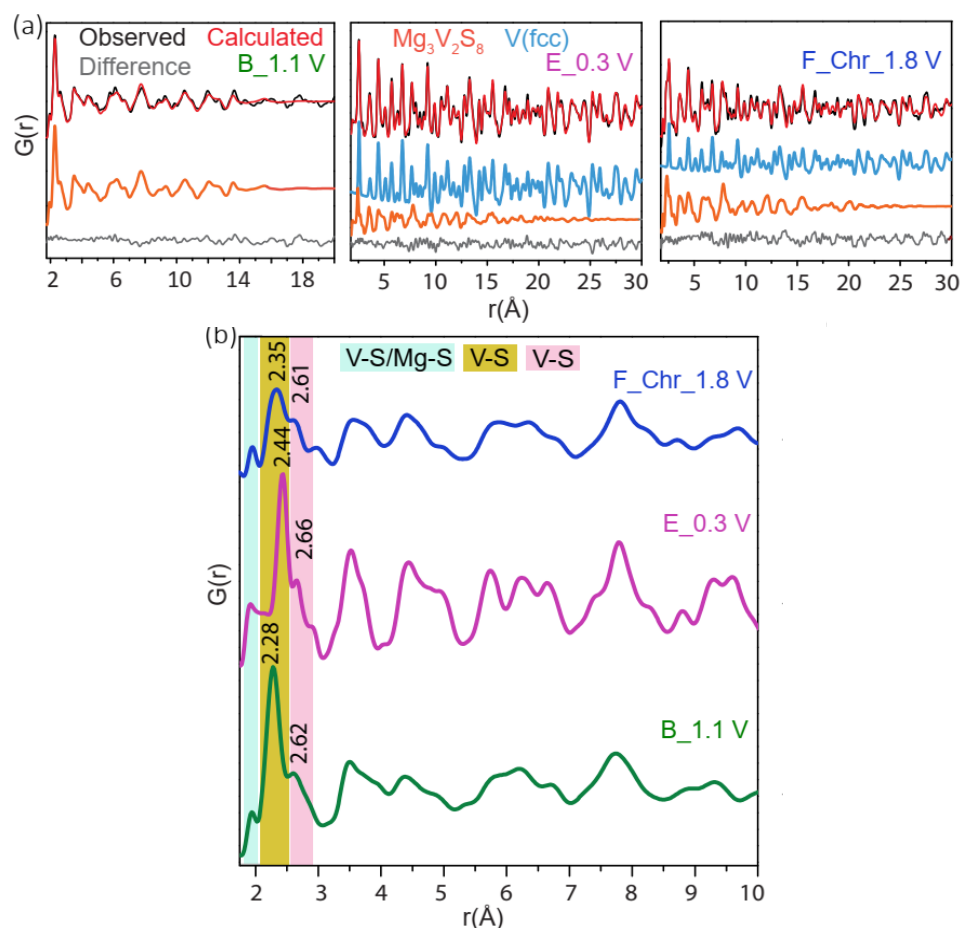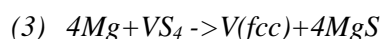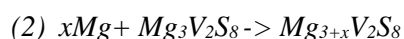


**Figure 8.** (a) Least squares refinements of *XPDF data of VS$_4$ at three different states of discharge and charge. Refinements were carried out in the range of 1.7-20.0 Å for sample B, and from 1.7-30.0 Å for samples E and F. Experimental, fitted and difference plots are shown in black, red and brown, respectively; individual correlations from* V (fcc) and $Mg_3V_2S_8$ are shown in blue and grey respectively. *(b) XPDF correlations of* $Mg_3V_2S_8$ *for samples B, E and F obtained* after subtracting the contribution of V metal from the total PDF data. *Coloured regions highlight the changes in selected correlations. The unit cell details corresponding to these changes are presented in Table S5 and Figure S12.*

## Discussion

$VS_4$ consists of $V^{4+}$ coordinated to S-S dimers, with V-S and S-S distances of 2.4 Å and 2.0 Å respectively. At the beginning of magnesiation (1.2-1.1 V, from A to B), the S-S dimers (formal charge of -1) are reduced to $S^{2-}$; this is accompanied by the oxidation of $V^{4+}$ to $V^{5+}$ leading to the formation of $Mg_3V_2S_8$ (eqn. 1). In contrast to a conventional intercalation reaction that accommodates inserted ions via redox of solely cations or anions, this process involves simultaneous cation and anion redox via an internal one electron transfer from $V^{4+}$ to $[S_2]^{2-}$ with the remaining 3e- (per mole of $VS_4$) provided from the external circuit (Figure 9). Since no prior report was found for a structure with composition close to $Mg_3V_2S_8$, we, therefore, used the *ab initio* structure generation method with the USPEX code to determine candidate structure. The lowest energy has layers of $V^{5+}$ tetrahedrally coordinated by $S^{2-}$. Empirically, the formation of this new intermediate is indicated by the appearance of new V pre edge peak and S edge peak characteristic of $T_d$ $V^{5+}$ and $S^{2-}$ environments, respectively, in addition to a new resonance observed by MATPASS $^{51}$V NMR. Refinement against XPDF data gives an average V-S bond distance in this intermediate of 2.28 Å.

During the discharge plateau at 1.1-0.9 V (from B to D), two reactions are observed to take place simultaneously (eqns. 2 and 3). First, reduction of $V^{5+}$ occurs, which is evidenced by both a decrease in the intensity of the V pre edge corresponding to $T_d$ $V^{5+}$ and by the decrease in intensity of the $^{51}$V NMR broad band signal in the $V^{5+}$ giving rise to an overall composition of $Mg_{3+x}V_2S_8$ (x > 0) at the end of the process (Eqn. 2, Figure 9). This $V^{5+}$ reduction redistributes charge amongst the V-S bonds in the V-S tetrahedra as evidenced by a slight increase in S K edge energy. Simultaneously $VS_4$ also undergoes conversion to V metal and MgS (Eqn. 3), seen in S XPS and V ssNMR. Our DFT-calculated potentials of $Mg_3V_2S_8$ formation (eqn. 1) and $VS_4$ conversion (eqn. 3) are 1.10 V and 1.04 V (w.r.t. $Mg^{2+}/Mg$) respectively (Table S5), allowing both reactions to proceed simultaneously.[37, 38]

(1) $\quad 3Mg + 2VS_4 \rightarrow Mg_3V_2S_8$

(2) $\quad xMg + Mg_3V_2S_8 \rightarrow Mg_{3+x}V_2S_8$

(3) $\quad 4Mg + VS_4 \rightarrow V(fcc) + 4MgS$

Upon discharging to 0.3 V (from D to E), the conversion reaction becomes dominant (eqn. 3), with V(fcc) formation confirmed by PDF and V NMR data, with significant changes in both the V and S XANES spectra confirming the sudden increase in V(fcc) and MgS content during this electrochemical process. PDF confirms the persistence of the remnant $Mg_{3+x}V_2S_8$ intermediate (formed during the discharge plateau at 1.1-0.9 V) to the end of discharge, consisting of mixed valent $V^{4+}/V^{5+}$ and $S^{2-}$ ions and consistent with an increase in average V-S bond lengths of 2.28 Å to 2.44 Å at the end of the discharge, indicative of transformation of $Mg_3V_2S_8$ to $Mg_{3+x}V_2S_8$. A weak absorption intensity at ~2469 eV in the S K XANES also persists until the end of discharge, further supporting this claim.
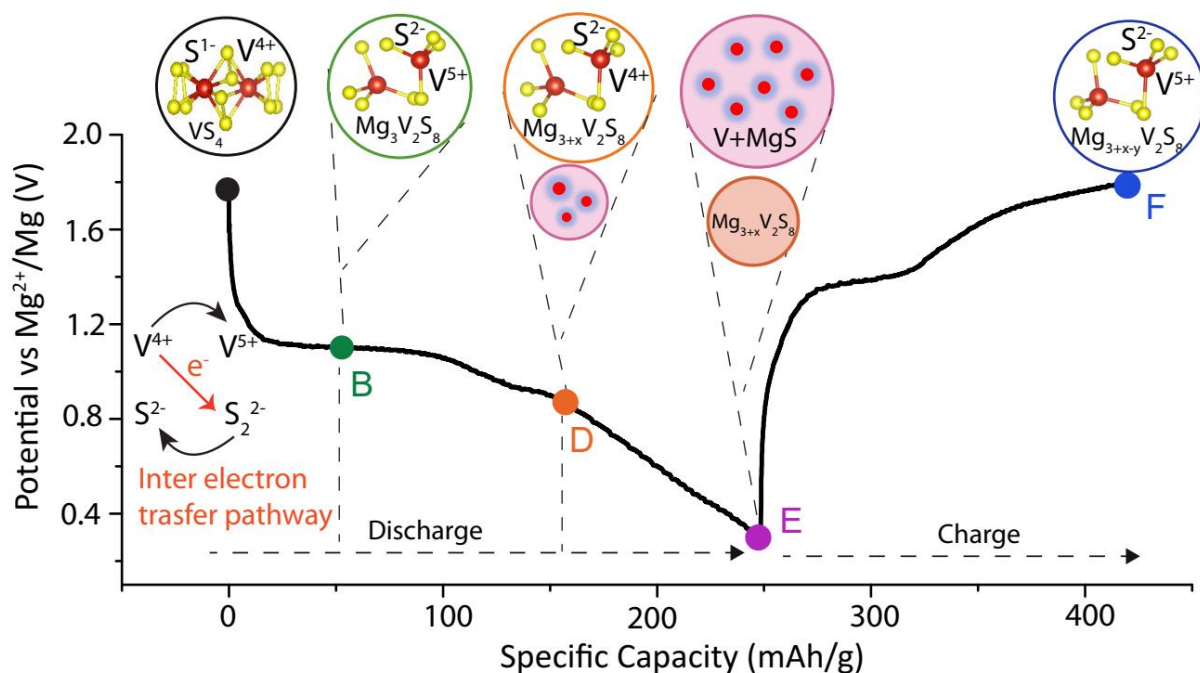
***Figure 9.*** *Schematic which summarises the redox processes occurred during (de)magnesiation of VS₄. The redox changes of V, S and the internal electron transfer pathway during process B are shown on the left. V and S atoms are shown as red and yellow balls, respectively, while the Mg atoms are omitted for simplification.*

The thermodynamically stable form of V is the bcc polymorph. Our DFT calculations show that the electrochemical potentials of $VS_4$ conversion to bcc and fcc polymorphs differ by only 0.04 V (Table S5). V(fcc) has previously been identified as a conversion product of Li/$VS_4$ electrochemistry by Britto *et al.*[17] Castro *et al.* also reported the conversion of V(bcc) to V(fcc) nanoparticles during the synthesis of δ-VN with ball milling under $N_2$.[28] Unusual metastable polymorphs have also been identified in earlier reports of Li and Mg ion conversion products such as in recent study by Nakayama et al., Mg/S chemistry has seen the formation of amorphous MgS in unusual metastable zinc blend phase rather than most stable rock salt phase at the end of discharge.[27, 39] In our case, the V metal is also amorphous and since it is nano in size, it is perhaps stabilised by a higher surface area.

$Mg_3V_2S_8$ reforms upon charging from E to F (Figure 9). This occurs in two ways: (i) through the partial reaction of V(fcc) and MgS and (ii) through the oxidation of $V^{4+}$ to $V^{5+}$ in remnant $Mg_{3+x}V_2S_8$ present at the end of discharge. Consumption of V(fcc) and MgS is confirmed through changes in V XANES, NMR, XPDF and S XPS. The reformation of $Mg_3V_2S_8$ is confirmed by spectral and PDF signatures that are similar to that seen upon the initial discharge to 1.1 V, i.e., a new pre edge characteristic of tetrahedral V in the V XANES and a new $^{51}V$ resonance in the MATPASS NMR spectrum. The presence of $S^{2-}$ is confirmed by a significant decrease in S edge energy along with the appearance of a new S XPS peak. The Mg content at the end of charge is slightly higher (~0.25 mol/f.u. of $VS_4$) than that is seen at 1.1 V during discharge (~0.17 mol/f.u. of $VS_4$), and the formula of the product at end of charge should be $Mg_{3+x-y}V_2S_8$. This is also reflected in the PDF analysis, as the average V-S bond distance obtained at the end of charge is ~ 2.35 Å (sample F, $Mg_{3+x-y}V_2S_8$; x-y >0), higher compared to

15

2.28 Å for sample B, $Mg_3V_2S_8$. There is no evidence of $VS_4$ reformation upon charging, with $^{51}V$ NMR spectra showing no increase in intensity of the characteristic resonances at 163 ppm assigned to V-V pairs.

$VS_4$ exhibits a hysteresis voltage of 0.75-0.80 V (Figure S13), which is comparable to other sulphide conversion materials.[40] The conversion of $VS_4$ to MgS and V involves a high degree of bond breaking and in order to reform $VS_4$ upon charging a large activation energy is required, causing the large voltage hysteresis. While it is possible that charging the sample above 1.8 V could result in the reformation of $VS_4$ the maximum oxidation potential was chosen based on the upper limit of the electrolyte stability window.[41]

Comparing the results here to those seen for lithiation, the analogous Li sulphide, $Li_3VS_4$, has not been chemically synthesized so far. During electrochemical intercalation of Li in $VS_4$, a $Li_3VS_4$ intermediate consisting of $VS_4$ tetrahedral units was also proposed to form; however, at this time no structural details of $Li_3VS_4$ are known.[17, 42] Other $M_3VS_4$ (M=Na, K) compounds have previously been synthesized,[43, 44] and contain the same $VS_4$ tetrahedral units as in $Mg_3V_2S_8$ (see Figure S14 for more structural details). However, both $Na_3VS_4$ (orthorhombic) and $K_3VS_4$ (tetragonal) have a close packed structure, unlike $Mg_3V_2S_8$, which has open channels in all three directions. Comparing $Mg_3V_2S_8$ and $VS_4$, both have a monoclinic unit cell, the $a$ and $b$ lattice parameters of $Mg_3V_2S_8$ are higher by +12% and 28% respectively while $c$ is lower by 2.66% (see Table S4). The unit cell parameters of the $Mg_3V_2S_8$ intermediate vary upon moving from the discharge to charge processes of $VS_4$, in particular, the $a$ and $b$ lengths expand significantly (Table S4).

The $Mg_3V_2S_8$ phases are highly disordered comprising a wide distribution of V/S oxidation states and variable V-S/ S-S bond lengths caused by the dynamic distribution of charges and distortion of the V-S tetrahedra. This is evidenced as $Mg_3V_2S_8$ shows broad S2p XPS bands (FWHM = 1.78 eV), and V pre-edge XANES peak (FWHM ~ 1.80-1.90 eV) much wider than that of $K_3VS_4$ (FWHM ~ 1.4 eV). XPDF shows that the V-S bond lengths of this compound lies between 2.28-2.35 Å, intermediate between V-S distances seen for crystalline $BaVS_3$ ($V^{4+}$) and $K_3VS_4$ ($V^{5+}$) (Table S6). Our DFT predicted a $^{51}V$ NMR shift of $Mg_3V_2S_8$ is 1522 ppm (Table S7). The observed MATPASS NMR resonance of the new phase is also very broad (between 300 and 1300 ppm).

Anionic redox chemistry has been observed in a variety of Li rich oxides including $Li_2Ru_{0.5}Sn_{0.5}O_2$, $Li_{1.2}Ni_{0.2}Mn_{0.6}O_2$, $Li_{1.3}Mn_{0.4}Nb_{0.3}O_2$, β-$Li_2IrO_3$ and $Li_4Mn_2O_5$[45-49], where the oxidation of $O^{2-}$ to superoxide ($O_2^-$) and/or peroxide ($O_2^{2-}$) is proposed to occur (during Li removal). The ability to harness both cationic and anionic redox chemistry leads to electrode materials with capacities that are amongst the highest known for intercalation compounds. However, to date, the combination of coupled reduction of TM cations (for example, $Ru^{6+} \rightarrow Ru^{5+}$) and the oxidation of $O^{2-}$ to $O^{1-}$ has only been proposed for $Li_2Ru_{0.5}Sn_{0.5}O_2$ which is possible due to the strong overlap between the O2p and Ru 4d bands,[47] although there are hints that this may also occur in some 3d systems. The overlap between d (cations) and sp (anions) orbitals increases further with an energy rise of the 3p anionic band when moving from oxides to sulphides. The more recent development of Li rich layered sulphides (e.g. $Li_2FeS_2$, $Li_{1.13}Ti_{0.57}Fe_{0.3}S_2$)[50-52] reinforces the importance of the $S^{2-}/S_2^{2-}$ and $TM^n/TM^{n+1}$ redox couple in improving capacity. In the case of Mg ion batteries, layered sulphides (operating via traditional cation redox) have shown better reversibility than oxides, despite the immense

challenges involved in developing suitable Mg electrolytes.[4-8] Elemental S has shown a higher capacity in initial cycles through S to MgS conversion, which involves S redox changes of 0 and -2.[53] However, transitional metal polychalcogenides[11, 54] in which a higher capacity can be achieved by utilising $S_2^{2-}/S^{2-}$ redox (in addition to the d electrons of metal ions), are largely unexplored for MIBs. By elucidating the fundamental electrochemical mechanisms of $VS_4$, this work paves the way for exploring the large family of transitional metal polychalcogenides for future practical battery applications.

## Conclusion

This report highlights the promise of $VS_4$ as a potential cathode for magnesium ion batteries, with high capacity and partial reversibility in long cycling. Using a suite of short-range characterization techniques in combination with theoretical structure prediction method, we have elucidated the structural changes that occur during Mg ion (de)insertion in $VS_4$. $VS_4$ undergoes an unusual combined cation-anion redox mediated intermediate formation followed by conversion as a result of Mg reaction. XPS reveals S-S bond breaking with a gradual reduction to $S^{2-}$ during Mg insertion, whereas S XANES distinguishes between the $S^{2-}$ of the intermediate phase and MgS. V XANES and $^{51}V$ ssNMR show changes in V redox states in between +4 and +5, including the formation of the metastable fcc polymorph of V metal. An evolutionary structure prediction algorithm was employed to predict the structure of an intermediate phase, $Mg_3V_2S_8$, that was identified on cycling. The structure was confirmed experimentally with structural refinement of the XPDF results. In conclusion, this work opens up the possibility of identifying family of materials which operate by anionic or combined cation-anionic redox reactions in the multivalent ion battery field with high capacities.

## Acknowledgements

## References.

1.      J. Muldoon, C. B. Bucur and T. Gregory, *Angew. Chem.*, 2017, **56**, 12064-12084.
2.      P. Canepa, G. Sai Gautam, D. C. Hannah, R. Malik, M. Liu, K. G. Gallagher, K. A. Persson and G. Ceder, *Chem. Rev.*, 2017, **117**, 4287-4341.
3.      M. Mao, T. Gao, S. Hou and C. Wang, *Chem. Soc. Rev.*, 2018, **47**, 8804-8841.

4.      X. Sun, P. Bonnick, V. Duffort, M. Liu, Z. Rong, K. A. Persson, G. Ceder and L. F. Nazar, *Energy Environ. Sci.*, 2016, **9**, 2273-2277.

5.      X. Sun, P. Bonnick and L. F. Nazar, *ACS Energy Lett.*, 2016, **1**, 297-301.

6.      M. Liu, A. Jain, Z. Rong, X. Qu, P. Canepa, R. Malik, G. Ceder and K. A. Persson, *Energy Environ. Sci.*, 2016, **9**, 3201-3209.

7.      H. D. Yoo, Y. Liang, H. Dong, J. Lin, H. Wang, Y. Liu, L. Ma, T. Wu, Y. Li and Q. Ru, *Nat. Commun.*, 2017, **8**, 1-10.

8.      Y. Liang, R. Feng, S. Yang, H. Ma, J. Liang and J. Chen, *Adv. Mater.*, 2011, **23**, 640-643.

9.      D. Aurbach, Z. Lu, A. Schechter, Y. Gofer, H. Gizbar, R. Turgeman, Y. Cohen, M. Moshkovich and E. Levi, *Nature*, 2000, **407**, 724.

10.     V. Duffort, X. Sun and L. F. Nazar, *Chem. Comm.*, 2016, **52**, 12458-12461.

11.     E. D. Grayfer, E. M. Pazhetnov, M. N. Kozlova, S. B. Artemkina and V. E. Fedorov, *ChemSusChem*, 2017, **10**, 4805-4811.

12.     D. Golodnitsky and E. Peled, *Electrochim. Acta*, 1999, **45**, 335-350.

13.     A. Débart, L. Dupont, R. Patrice and J.-M. Tarascon, *Solid State Sci.*, 2006, **8**, 640-651.

14.     R. Sun, Q. Wei, Q. Li, W. Luo, Q. An, J. Sheng, D. Wang, W. Chen and L. Mai, *ACS Appl. Mater. Interfaces*, 2015, **7**, 20902-20908.

15.     X. Xu, S. Jeong, C. S. Rout, P. Oh, M. Ko, H. Kim, M. G. Kim, R. Cao, H. S. Shin and J. Cho, *J. Mater. Chem. A*, 2014, **2**, 10847-10853.

16.     C. S. Rout, B.-H. Kim, X. Xu, J. Yang, H. Y. Jeong, D. Odkhuu, N. Park, J. Cho and H. S. Shin, *J. Am. Chem. Soc.*, 2013, **135**, 8720-8725.

17.     S. Britto, M. Leskes, X. Hua, C.-A. Hébert, H. S. Shin, S. Clarke, O. Borkiewicz, K. W. Chapman, R. Seshadri, J. Cho and C. P. Grey, *J. Am. Chem. Soc.*, 2015, **137**, 8499-8508.

18.     R. Allmann, I. Baumann, A. Kutoglu, H. Rösch and E. Hellner, *Naturwissenschaften*, 1964, **51**, 263-264.

19.     Y. Wang, Z. Liu, C. Wang, X. Yi, R. Chen, L. Ma, Y. Hu, G. Zhu, T. Chen, Z. Tie, J. Ma, J. Liu and Z. Jin, *Adv. Mater*, 2018, **30**, 1802563.

20.     A. R. Oganov, A. G. Kvashnin and G. Saleh, *Computational Materials Discovery: Dream or Reality?*, 2018, 1-14, DOI: 10.1039/9781788010122-9781788000001.

21.     https://xpssimplified.com/elements/sulfur.php.

22.     J. Wong, F. Lytle, R. Messmer and D. Maylotte, *Phys. Rev. B*, 1984, **30**, 5596.

23.     S. Sutton, J. Karner, J. Papike, J. Delaney, C. Shearer, M. Newville, P. Eng, M. Rivers and M. J. G. e. C. A. Dyar, *Geochimica et Cosmochimica Acta*, 2005, **69**, 2333-2348.

24.     M. Ostrooumov, Y. Taran, M. Arellano-Jiménez, A. Ponce and J. Reyes-Gasga, *Revista Mexicana de Ciencias Geológicas*, 2009, **26**, 600-608.

25.     D. A. McKeown, I. S. Muller, K. S. Matlack and I. L. Pegg, *J. non-cryst solids*, 2002, **298**, 160-175.

26.     J. Wong and G. A. Slack, *J. Solid State Chem.*, 1986, **61**, 203-211.

27.     M. M. Butala, M. Mayo, V. V. T. Doan-Nguyen, M. A. Lumley, C. Göbel, K. M. Wiaderek, O. J. Borkiewicz, K. W. Chapman, P. J. Chupas, M. Balasubramanian, G. Laurita, S. Britto, A. J. Morris, C. P. Grey and R. Seshadri, *Chem. Mater.*, 2017, **29**, 3070-3082.

28.     V. López-Flores, M. A. Roldán, C. Real, A. M. Páez and G. R. Castro, *J. Appl. Phys.*, 2008, **104**, 023519.

29.     I. Hung, L. Zhou, F. Pourpoint, C. P. Grey and Z. Gan, *J. Am. Chem. Soc.*, 2012, **134**, 1898-1901.

30.     D. M. Halat, R. Dervişoğlu, G. Kim, M. T. Dunstan, F. Blanc, D. S. Middlemiss and C. P. Grey, *J. Am. Chem. Soc.*, 2016, **138**, 11958-11969.

31.     Y. P. Zhang and R. H. J. I. C. Holm, *Inorg. Chem.*, 1988, **27**, 3875-3876.

32.     Y. T. Hayden and J. O. J. I. c. a. Edwards, *Inorganica chimica acta*, 1986, **114**, 63-69.

33.     https://materialsproject.org/.

34. A. R. Oganov and C. W. Glass, *J. Chem. Phys.*, 2006, **124**, 244704.
35. A. R. Oganov, A. O. Lyakhov and M. Valle, *Acc. Chem. Res.*, 2011, **44**, 227-237.
36. A. O. Lyakhov, A. R. Oganov, H. T. Stokes and Q. Zhu, *Comp. Phys. Commun.*, 2013, **184**, 1172-1182.
37. C. Ling, R. Zhang, T. S. Arthur and F. Mizuno, *Chem. Mater.*, 2015, **27**, 5799-5807.
38. D. C. Hannah, G. Sai Gautam, P. Canepa and G. Ceder, *Adv. Energy Mater.*, 2018, **8**, 1800379.
39. Y. Nakayama, R. Matsumoto, K. Kumagae, D. Mori, Y. Mizuno, S. Hosoi, K. Kamiguchi, N. Koshitani, Y. Inaba and Y. Kudo, *Chem. Mater.*, 2018, **30**, 6318-6324.
40. J. Cabana, L. Monconduit, D. Larcher and M. R. Palacin, *Adv. Mater*, 2010, **22**, E170-E192.
41. D. Lv, T. Xu, P. Saha, M. K. Datta, M. L. Gordin, A. Manivannan, P. N. Kumta and D. Wang, *J. Electrochem. Soc.*, 2013, **160**, A351-A355.
42. K. Shimoda, K. Koganei, T. Takeuchi, T. Matsunaga, M. Murakami, H. Sakaebe, H. Kobayashi and E. Matsubara, *RSC Adv.*, 2019, **9**, 23979-23985.
43. J. Van den Berg and R. De Vries, 1964.
44. A. T. Harrison and O. W. Howarth, *J. Chem. Soc., Dalton Trans.*, 1986, 1405-1409.
45. P. E. Pearce, A. J. Perez, G. Rousse, M. Saubanère, D. Batuk, D. Foix, E. McCalla, A. M. Abakumov, G. Van Tendeloo and M.-L. Doublet, *Nat. mater.*, 2017, **16**, 580.
46. H. Koga, L. Croguennec, M. Ménétrier, K. Douhil, S. Belin, L. Bourgeois, E. Suard, F. Weill and C. Delmas, *J. Electrochem. Soc.*, 2013, **160**, A786-A792.
47. M. Sathiya, G. Rousse, K. Ramesha, C. Laisa, H. Vezin, M. T. Sougrati, M.-L. Doublet, D. Foix, D. Gonbeau and W. Walker, *Nat. Mater.*, 2013, **12**, 827.
48. M. Freire, N. Kosova, C. Jordy, D. Chateigner, O. Lebedev, A. Maignan and V. Pralong, *Nat. Mater.*, 2016, **15**, 173.
49. N. Yabuuchi, M. Takeuchi, M. Nakayama, H. Shiiba, M. Ogawa, K. Nakayama, T. Ohta, D. Endo, T. Ozaki and T. Inamasu, *Proc. Natl. Acad. Sci. U.S.A.*, 2015, **112**, 7650-7655.
50. C. J. Hansen, J. J. Zak, A. J. Martinolich, J. S. Ko, N. H. Bashian, F. Kaboudvand, A. Van der Ven, B. C. Melot, J. Nelson Weker and K. A. See, *J. Am. Chem. Soc.*, 2020.
51. A. Sakuda, T. Takeuchi, K. Okamura, H. Kobayashi, H. Sakaebe, K. Tatsumi and Z. Ogumi, *Sci. Rep.*, 2014, **4**, 1-5.
52. S. Saha, G. Assat, M. T. Sougrati, D. Foix, H. Li, J. Vergnet, S. Turi, Y. Ha, W. Yang and J. Cabana, *Nature Energy*, 2019, **4**, 977-987.
53. H. S. Kim, T. S. Arthur, G. D. Allred, J. Zajicek, J. G. Newman, A. E. Rodnyansky, A. G. Oliver, W. C. Boggess and J. Muldoon, *Nat. Commun.*, 2011, **2**, 1-6.
54. J. Rouxel, *Chem. Eur. J.*, 1996, **2**, 1053-1059.

**Exploring the Peierls-Distorted Vanadium Sulphide as A Rechargeable Mg-Ion Cathode**

Sunita Dey,[a] Jeongjae Lee,[a] Sylvia Britto,[a,b] Joshua M. Stratford,[a] Giannantonio Cibin,[b] Evan N. Keyzer,[a] Simon J. Cassidy,[c] Mahmoud Elgaml [c], Matthew T. Dunstan,[a] and Clare P. Grey[*, a]

[a]*Department of Chemistry, University of Cambridge, Lensfield Road, Cambridge, CB2 1EW, UK*
[b]*Diamond Light Source, Harwell Science and Innovation Campus, Didcot, UK*
[c]*Department of Chemistry, University of Oxford, South Parks Road, Oxford, OX1 3QR, UK*
*[*cpg27@cam.ac.uk](cpg27@cam.ac.uk)*

*Fax: (+44)1223336362; Tel: (+44)1223336509*

**Materials and Methods.**

$VS_4$-reduced graphene oxide (rGO) powder was synthesized following the previous report of Rout. et.al.[16] The composites have 3 wt% rGO content. The particle sizes are in the range of 100-500 nm.[16] $LiVS_2$ and $K_3VS_4$, which were used as model compounds for the S and V XANES measurements, were prepared by sealed tube method following the previous report by Britto et al.[17] $K_3VS_4$ was synthesized by grinding together stoichiometric quantities of $K_2S$, V, and S and heating the mixture in a sealed tube at 650 °C for 20 h.[24] Similarly, $LiVS_2$ was prepared by heating the resultant mixture of $Li_2S$, V, and S at 750 °C for 20 h.[55] Another model compound MgS was synthesized by heating the $MgSO_4$ (≥ 99.5%) powder in the stream of $CS_2$-aerosolised Ar at 800 °C for 4 hrs, the powder was cooled down, transferred to the glove box, grounded and heated again in the stream of $CS_2$-aerosolised Ar. S powder was received from Sigma-Aldrich.

*Electrode preparation*. $VS_4$ was mixed homogenously with Ketjen Black and PVDF (weight ratio of 80:10:10) using N-Methyl-2-pyrrolidone (NMP, anhydrous, Sigma-Aldrich) and casted on copper foil in thickness of 150 µm. Film was dried at 60°C under vacuum before punching out $VS_4$ cathode of area 1.27 cm$^2$ with loading ~ 3 mg/cm$^2$. Mg ribbon (Sigma Aldrich) was polished by blade to remove the MgO layer and cut into pieces of ˜8 mm X 3 mm X 0.2 mm to fit in 2032 type cells. A 0.25 (M) solution $Mg(AlCl_2EtBu)_2$ in dry THF (supplied by Sigma Aldrich, ≥ 99.0%, re distilled in lab and stored over molecular sieves showing final $H_2O$ content of ˜12 ppm by Karl Fisher titration) was used as the electrolyte. Standard stainless steel 2032 coin cells (Cambridge Energy Solutions) were assembled inside the Ar glovebox with borosilicate glass fibre separator (Whatman) soaked on 150 µl electrolyte, 0.5 mm thick spacer, conical spring, plastic gasket and Mg metal as counter electrode. All electrochemical measurements were conducted at 293±2 K using Lanhe battery cycler (Wuhan Land Electronics Co. Ltd.). Prior to ex situ measurements batteries were dissembled inside Ar glove box, cycled films were rinsed three times with THF and dried in glove box prechamber (under vacuum) for 30 mins.

*X-ray photoelectron spectroscopy (XPS).* XPS was carried out at Harwell Campus, UK. Thermo Scientific K-Alpha XPS system with monochromated micro focused Al-Kα X ray source of energy 1468.7 eV was used at a power of 72W (12 kV x 6 mA). The instrument was equipped with 180°,

double focusing, and hemispherical analyzer with 128-channel detector. Fixed Analyzer Transmission mode with pass energy of 40 eV was used. Samples were adhered to a conductive carbon film taped onto air tight transfer chamber (designed by Themo Fisher Scientific, total loading area 60 X 60 mm) equipped with X-ray-transparent windows and were brought down to a measurement pressure of $10^{-8}$ mbar. Instrument is equipped with Monatomic and Gas Cluster Ion Source (MAGCIS). Before recording the spectra, cluster cleaning was carried out for 1 min in order to remove the surface contaminations. The clustering uses energy of 4 keV (nearly a cluster of 4000 Ar atoms carrying energy of 1eV/atom). The spot size of measurement was 400 μm with step size of 5 μm. Along with high resolution survey scan, energy specific spectra of S2p, V2p and Mg2p were recorded by dedicated scanning (step size 0.1 eV/min) over the energy ranges of 155-168 eV, 510-540 eV and 46-55 eV respectively. Data processing, background correction (used Shirley function) and peak fitting (used Gaussion-Lorentzian functions) were performed by CasaXPS software (version 2.3.15). Surface charging shifts the true binding energy of electrons; C 1s photoelectron peak position of 284.8 eV is used as an internal reference.

***NMR Analysis.*** All the experiments are performed in BrukerAvance 500 MHz (11.7 T) spectrometer operating at a $^{51}$V Larmor frequency of 131.7 MHz at room temperature. Samples were packed into $ZrO_2$ rotor inside the Ar filled glove box. Bruker probes of 1.3 mm and 2.5 mm are used for magic angle spinning (MAS) of 25 kHz and 50 kHz respectively. An echo sequence with a π/2 pulse length of 1.5 μs and recycle delay of 5 s was used. All the spectra were referenced using solid $NH_4VO_3$ (Sigma-Aldrich, > 99%) resonating at −565.5 ppm as secondary reference.[56] The carrier frequency has been fixed to 163 ppm and 5600 ppm for recording $VS_4$ and V spectra respectively. Bruker Topspin (version 4.0.7) was used for raw data processing.

Magic angle turning and phase adjusted sideband separation (MATPASS) NMR experiments were also performed at 11.7 T and were rotor-synchronized at a MAS rate of 50 kHz.[29] A series of five π/2 pulses with a pulse length of 1.5 μs was employed. A total of eight $t_1$ increments was recorded in each experiment with the recycle delay of 0.5 s.

***X-ray absorption spectroscopy (XAS).*** Ex situ XAS was carried out at beamline B18 (bending magnet) at the Diamond Light Source (DLS), UK. V K and S K edge spectra were measured at ambient temperature in transmission mode and total electron yield (TEY) mode respectively. The energy scans were done above and below the absorption edges of V (~5465eV) and S (~2472 eV) over the span of 950 eV (step size 0.22 eV) and 400 eV (step size 0.15 eV) respectively. For V K edge transmission mode measurements, around 5 mg of active material was scrapped off the film, grounded homogenously with dried cellulose (approx. 25-30 mg), pressed into 8 mm-diameter pellets (thickness of ~ 1 mm) and finally transferred in a custom-built (DLS) transfer chamber with X-ray-transparent windows. For S TEY measurements, cathode films were directly adhered to the transfer chamber with conductive tape. Argon in the measurement chamber was purged with He in order to minimise background absorption of the incident X-rays. The samples were measured at overpressure of He to avoid the air exposure. Beam size was 200 μm X 250 μm. Three consecutive spectra were collected from each sample to improve the signal-to-noise ratio and to ensure no beam damage or sample instability. Ionization chamber detectors are used for transmission mode measurements. Simultaneous measurement of a standard V foil and S powder was performed for energy calibration during the XAS recordings. XAS of all the model compounds were recorded under

similar conditions. Background correction, energy calibration, data merging, analysis and peak fitting were performed within the Athena program in the Demeter package running IFEFFI.[57]

***Pair Distribution Function Analysis (PDF).*** PDF measurements were performed at beamline I15 at Diamond Light Source, UK at X ray transmission mode. Samples were packed in borosilicate capillary (diameter~ 1.0 mm) and sealed with adhesive. Background measurements were taken in an identical empty capillary. Typical exposure time was 100 sec per scan. Measurements were performed with X-ray beam of energy of 76 keV ($\lambda$=0.1631 Å). An amorphous silicon area detector (PerkinElmer) had recorded total scattering data with large value of momentum transfer ($Q_{max}$~ 41.2 Å). The data were converted to intensity vs Q using FiT2D software.[58] All standard corrections including background, Compton scattering and detector effects were applied flowed by Fourier transformation to get G(r) using PDFGetX2 software.[59] Structural refinements have been performed in PDFGUI.[60]

No attempt was made to add the contributions from the binder and carbon as they are weak X ray scatters. A spherical particle approximation was used to model particle size and the ordering length scale was used to get the particle sizes for phases with limited correlations. As obtained $R_w$ value was implemented as a measure of goodness of fit. $R_w$ value greater than 15 % are usual in PDF results, even in well crystalline materials. PDF refinements producing much higher $R_w$ than typical XRD Rietveld refinement as both the methods uses different functions to solve the structure.[61, 62]

***Computation.*** Potential stable phases corresponding to the composition $Mg_3V_2S_8$ (*i.e.* a full reduction of sulphur to $S^{2-}$) were searched using the evolutionary method as implemented in the USPEX code.[34-36] Ionic relaxations of the generated structures were performed within the framework of Density Functional Theory (DFT) utilizing the Perdew-Burke-Ernzerhof (PBE) functional as implemented in the VASP code.[63, 64] Projector-augmented wave pseudopotentials with the following valence electrons were used: 2s (Mg), 3s (V), and 2p (S). A plane-wave energy cutoff of 340 eV and *k*-point resolution of <0.05 Å$^{-1}$ was used for the final energy calculation. The starting generation consisted of 50 structures consisting of up to 5 formula units (52 atoms) in all possible space groups except the *P1.* A total of 64 generations were produced with 50 structures in each generation; the minimisation was deemed complete when a structure was the lowest enthalpy structure for 30 generations. The proportions of evolutionary operators were adjusted automatically as implemented in the USPEX code. Potentials for the electrochemical (insertion and) conversion reactions were calculated within the same theoretical framework while fully relaxing the structures. Formation energy calculations were also performed under the same theoretical framework.

Phonon calculation on the $Mg_3V_2S_8$ structure was performed using the phonopycode[65] employing the finite-displacement method. A 52-atom supercell was used with a 2×2×2 Monkhorst-Pack grid and an increased plane-wave energy cutoff of 550 eV.

NMR chemical shifts of the respective phases were calculated using the CASTEP code[66] employing the GIPAW algorithm. CASTEP default ultrasoft pseudopotentials were used with a plane-wave energy cutoff of 700 eV and Monkhorst-Pack*k*-point resolution of <0.05 Å$^{-1}$. The calculated values of shielding were referenced to $NH_4VO_3$ which showed an experimental $^{51}V$ shift of -565.5 ppm.[56]

## Section 1. Supporting figures of electrochemistry



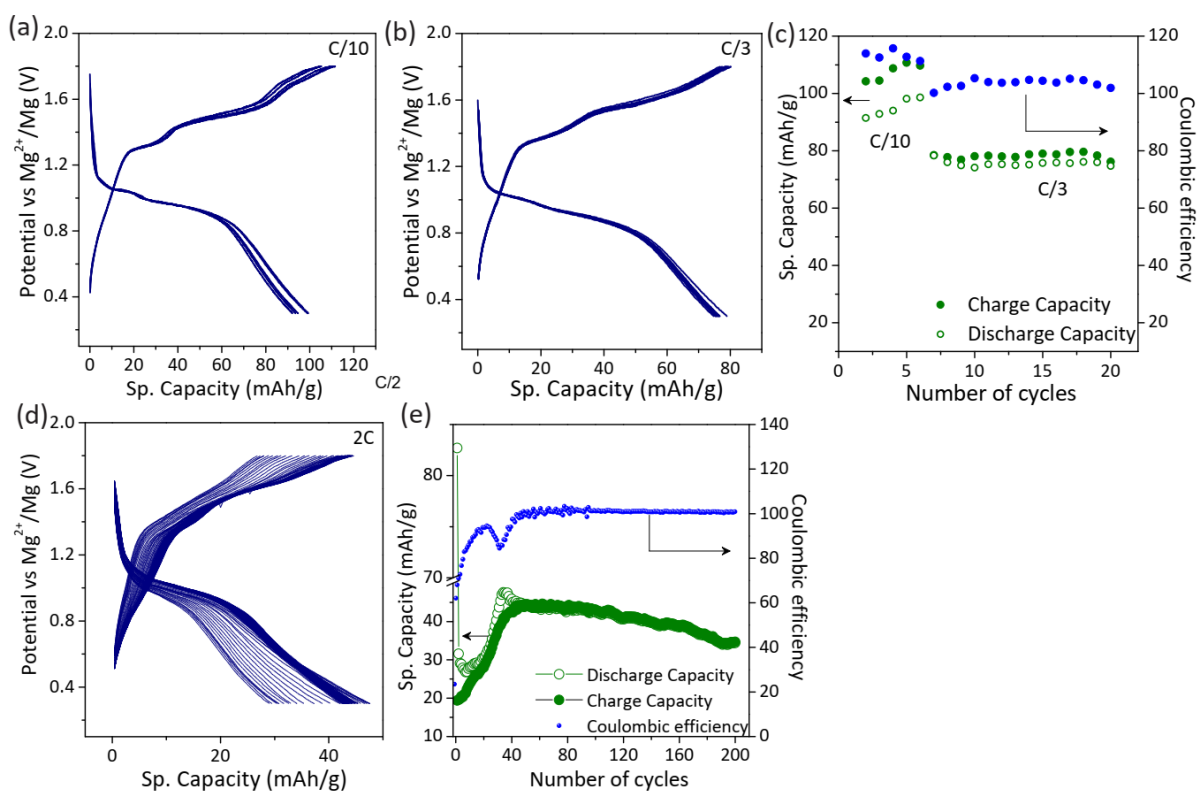**Figure S1.** *VS₄ is galvanostatically cycling at rate of (a) C/10, (b) C/3 and (d) 2C. The variation of discharge-charge specific capacity and Coulombic efficiency with cycle numbers are shown in figures c and e.*
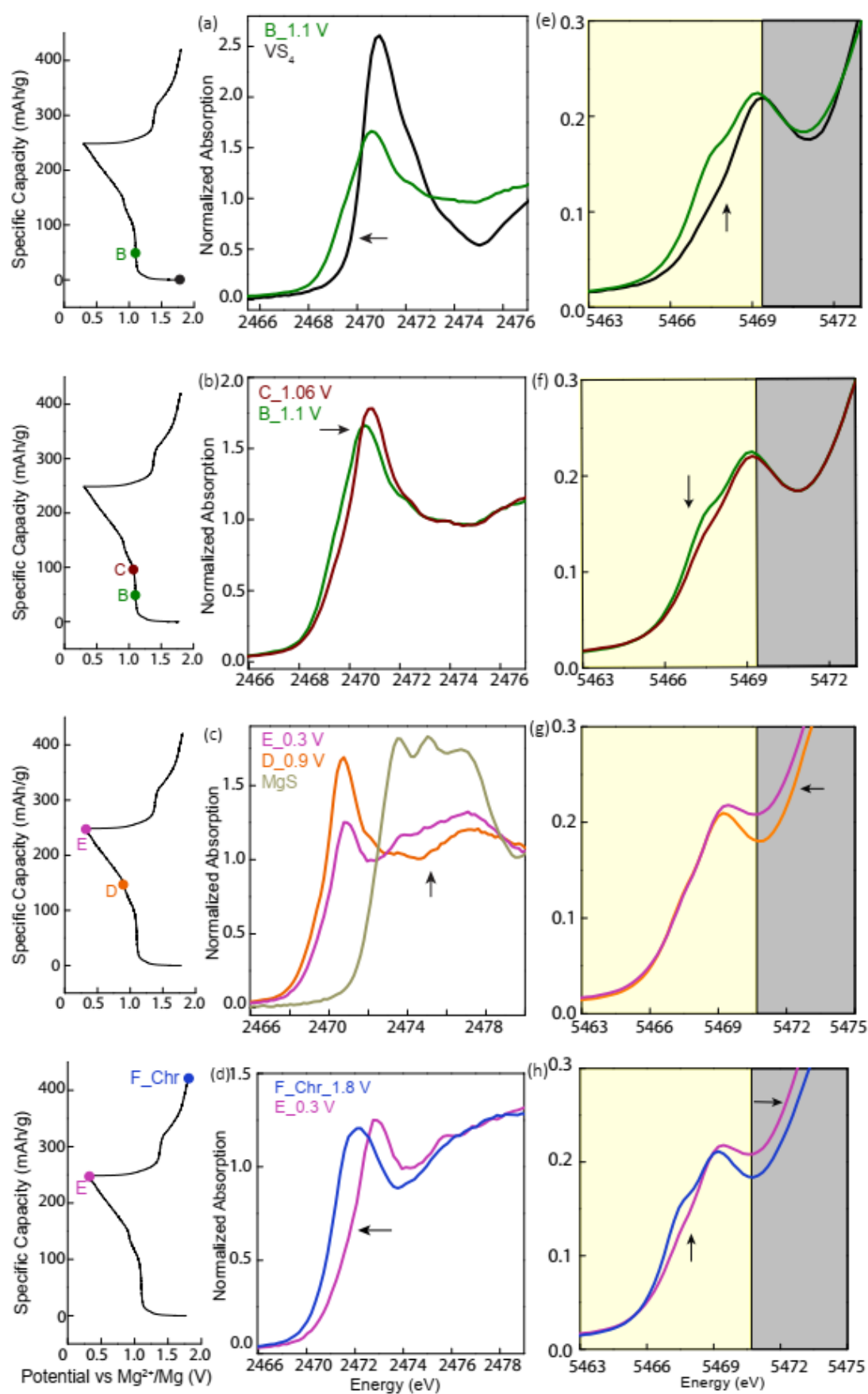
## Section 2. XANES supporting figures

**Figure S2.** *(a-d) S and (e-h) V K edge XANES spectra of VS$_4$ at various states of discharge and charge. Sudden changes in absorption position and intensity are marked by arrows.*
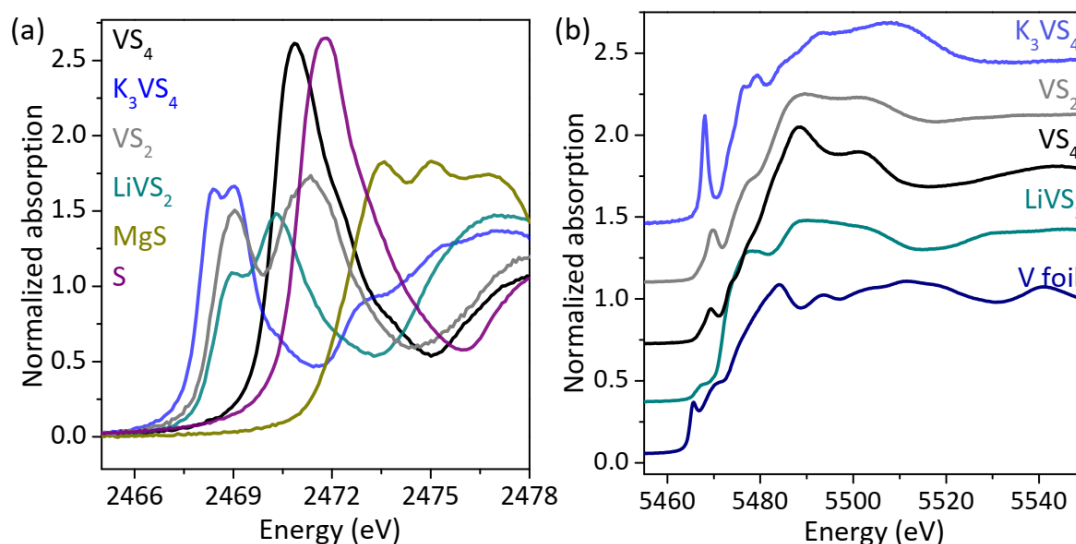


**Figure S3.** *(a) Normalized S K edge and (b) V K edge XANES spectra of model compounds: LiVS$_2$ (V$^{3+}$, S$^{2-}$), VS$_2$ (V$^{4+}$, S$^{2-}$), K$_3$VS$_4$ (V$^{5+}$, S$^{2-}$), VS$_4$ (V$^{4+}$, S$^{1-}$), MgS (S$^{2-}$), S(0) and V(0).*
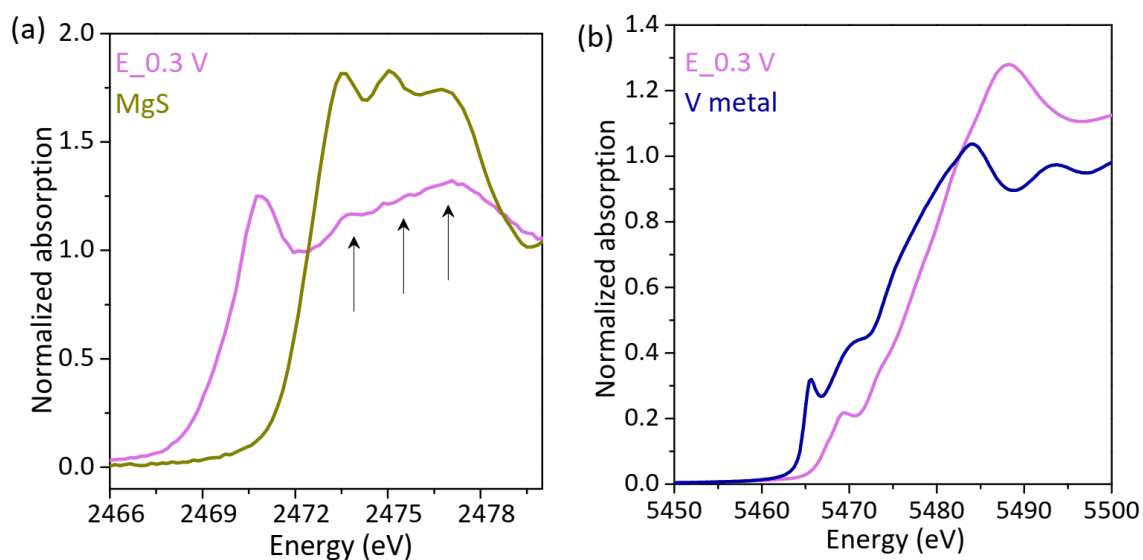


**Figure S4.** *(a) Normalized S K edge XANES spectra of sample E (0.3 V discharged sample) is presented in comparison to model compound MgS. The high energy region of sample E has three distinct energy features due to constructive resonances (pointed by arrows), which closely matches with the absorption features of MgS. (b) Normalized V K edge XANES spectra of sample E (0.3 V discharged sample) in comparison to commercially available body centred cubic V metal.*
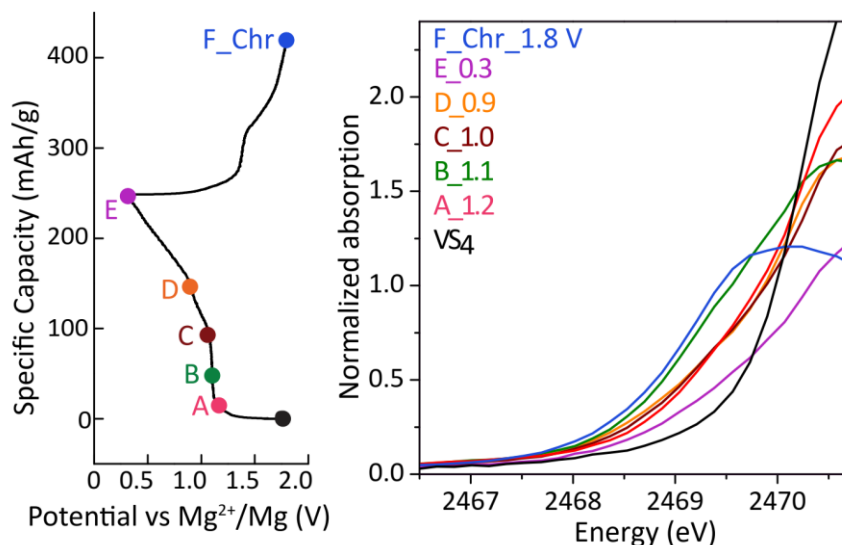
25

**Figure S5.** *S K edge XANES spectra of VS$_4$ at different states of discharge and charge to show the absorption in the edge rise energy ranges between 2467-2471 eV.*
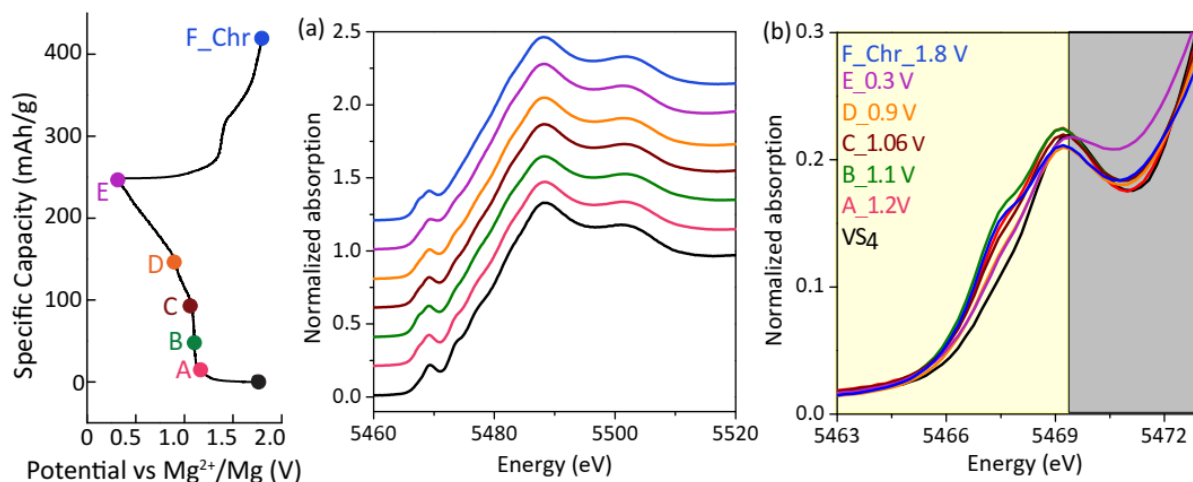


**Figure S6.** *(a) V K edge XAS (5460-5520 eV) spectra of VS$_4$ at different states of discharge and charge (spectra are vertically offset by 0.2) and (b) V K edge XANES spectra of VS$_4$ at different states of discharge and charge.*

**Table S1:** *Peak area of V$^{5+}$ and V$^{4+}$ in V pre edge XANES spectra and their ratio. Peaks are fitted using Gaussian function. The area is calculated after background subtraction. (\*) In VS$_4$, the area for V$^{5+}$area appears due to crystal field splitting rather than true oxidation. (\*\*) Sample E has contribution from V(fcc), so the calculation could have some error.*

| Sample | Peak area of V$^{4+}$ | Peak area of V$^{5+}$ | Area ratio (V$^{5+}$/ V$^{4+}$) |
|--------|----------------------|----------------------|-------------------------------|
| VS$_4$ | 76.14 | 15.40* | 0.2 |

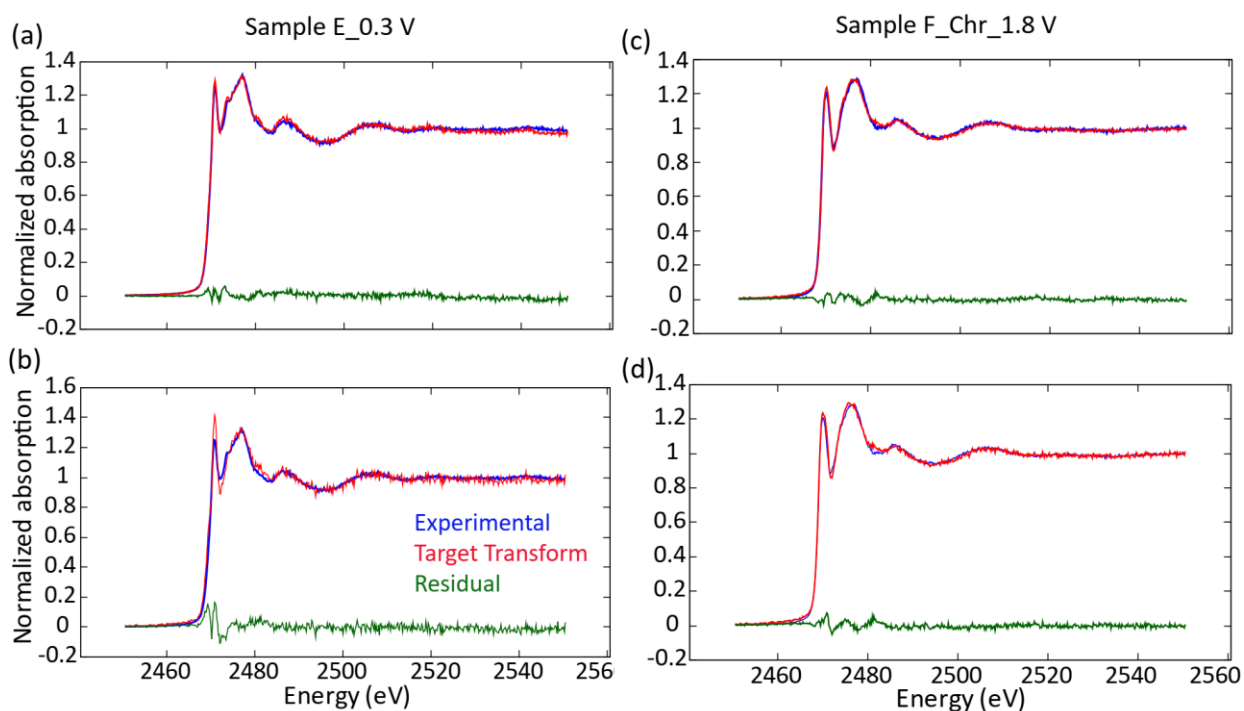| | | | |
|---|---|---|---|
| A_1.2 V | 67.61 | 32.40 | 0.47 |
| B_1.1 V | 60.60 | 39.40 | 0.61 |
| C_1.06 V | 67.74 | 32.25 | 0.47 |
| D_0.9 V | 70.67 | 29.33 | 0.41 |
| E_0.3 V | 79 | 21 ** | 0.26 |
| F_Chr_1.8 V | 60 | 40 | 0.66 |



**Figure S7.** *Target transform Principle component analysis results for sample E and F in 1st and 2nd column respectively. Two sets of principle components are generated by VS4, sample B and sample C with or without MgS (4 and 3 component PCA). Samples E and F were used as the target. Four components PCA consist of VS4, sample B, C and MgS (upper row; a and c). Three components PCA don't contain MgS (down row; b and d). Blue, red and green spectra are recorded, generated and residual plot respectively. Sample B and C are carefully chosen as they contain different V-S environments. Target transform is qualitative method, doesn't provide any quantitative evaluation.*
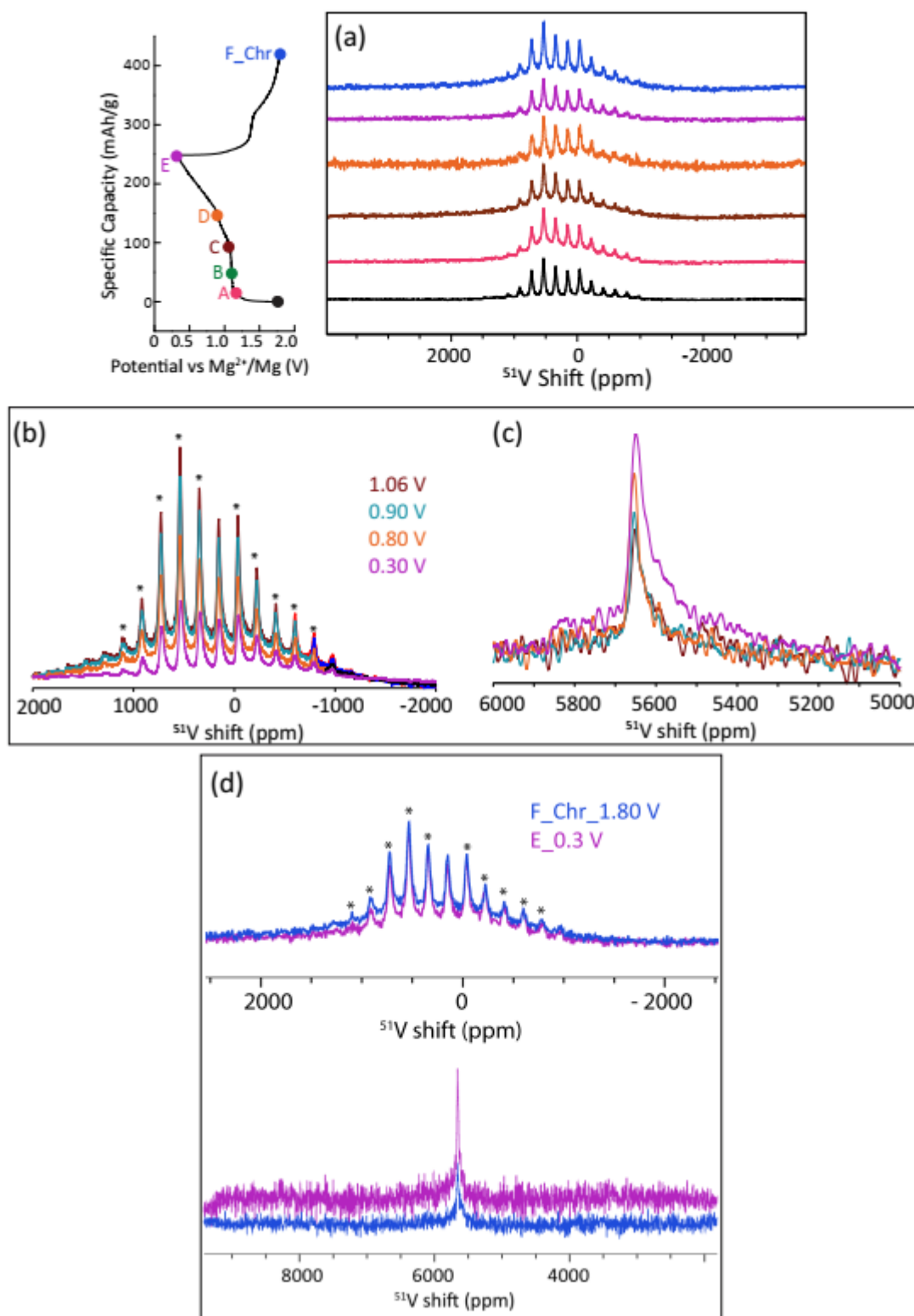
**Figure S8.** $^{51}V$ NMR spectra of (a) $VS_4$ recorded during first charge-discharge cycle at lower Magic angle spinning (MAS) speed of 25 KHz acquired at 11.7 T magnet. Isotropic peak is marked by line.

*Asterisk denotes the side bands. No extra peak appears on cycling at this MAS, besides the peaks inherent of VS₄. ⁵¹V NMR intensity of (b) VS₄ decreases and (c) V (fcc) metal increases gradually during first discharge processes. (d) ⁵¹V NMR intensity of VS₄ remain similar (top) and V (fcc) metal decreases (bottom) on moving from the end of discharging (E_0.3 V) to charging (F_1.8 V). All the spectra are normalized w.r.t. number of scans and weight of the sample.*
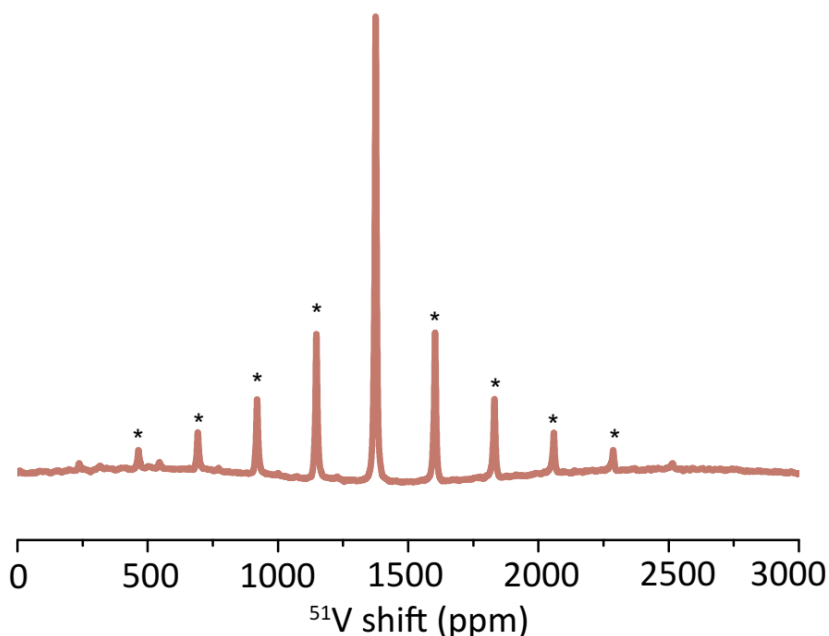


**Figure S9.** *⁵¹V NMR of K₃VS₄ (model compound) measured at 9.4 T field strength. Asterisk denotes the side bands.*

### Section 4. Supporting figures of XPDF and structural calculations

**Table S2.** *Structural parameters of pristine VS₄ obtained from PDF refinement ($R_w = 35.5\%$) in comparison with literature report (ICSD 16797).*

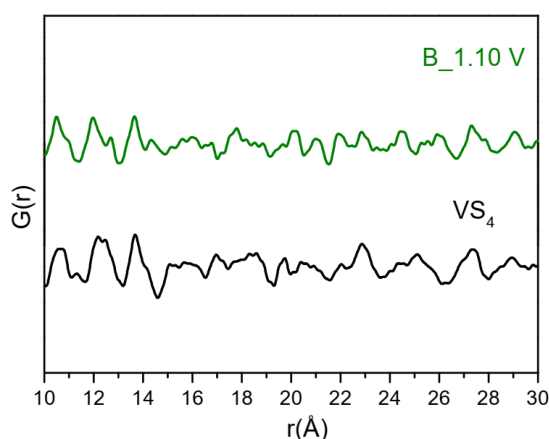|  | Literature Structure | PDF refinement |
|---|---|---|
| $a/\text{Å}$ | 6.780 | 6.726 |
| $b/\text{Å}$ | 10.42 | 10.466 |
| $c/\text{Å}$ | 12.11 | 12.087 |
| $\beta/^\circ$ | 100.8 | 100.7 |

**Figure S10.** *High r (7-50 Å) PDF correlations of pristine and 1.1 V discharged VS$_4$.*

**Table S3.** *Proposed reaction pathways for the formation of various ternary Mg-V-S compositions as a product of the reactions between VS$_4$ and Mg. Ternary Mg-V-S composition are selected from materials project databases.[33] These reaction pathways are simulated and calculated voltages are close to the VS$_4$ discharge plateau. The oxidation state of S is -2 and V is either +4 or lower in the Mg-V-S compositions.*

| Ternary Mg-V-S materials | E above hull (eV) | Proposed reaction | Voltage (V) |
|---|---|---|---|
| $Mg(VS_2)_4$ | 0.057 | $9Mg + 4VS_4 \rightarrow Mg(VS_2)_4 + 8MgS$ | 1.33 |
| $Mg(VS_2)_2$ | 0.117 | $5Mg + 2VS_4 \rightarrow Mg(VS_2)_2 + 4MgS$ | 1.28 |
| $MgVS_3$ | 0.222 | $2Mg + VS_4 \rightarrow MgVS_3 + MgS$ | 1.11 |
| $MgV_2S_5$ | 0.261 | $4Mg + 2VS_4 \rightarrow MgV_2S_5 + 3MgS$ | 1.13 |

**Table S4.** *Unit cell details of USPEX-generated Mg$_3$V$_2$S$_8$ structure.*

Space group H-M "C 1 c 1"; Cell lengths are $a$ = 7.604(5) Å, $b$ = 13.3501(6) Å, $c$ = 12.3812(1); Cell angles are $\alpha=\gamma$= 90.0°, $\beta$=106.68(8) °; Unit cell volume is 1204.012(9) Å$^3$

| Label | Symbol | Multiplicity | Wyckoff label | x | y | z | Occupancy |
|---|---|---|---|---|---|---|---|
| Mg1 | Mg | 4 | a | 0.08233 | 0.21462 | 0.23908 | 1.0000 |
| Mg2 | Mg | 4 | a | 0.33120 | 0.46327 | 0.23354 | 1.0000 |
| Mg3 | Mg | 4 | a | 0.85245 | 0.46201 | 0.28750 | 1.0000 |
| V1 | V | 4 | a | 0.20328 | 0.37418 | 0.43921 | 1.0000 |
| V2 | V | 4 | a | 0.74557 | 0.45431 | 0.05282 | 1.0000 |

| S1 | S | 4 | a | 0.78121 | 0.39932 | 0.62034 | 1.0000 |
|----|---|---|---|---------|---------|---------|--------|
| S2 | S | 4 | a | 0.51405 | 0.11872 | 0.61756 | 1.0000 |
| S3 | S | 4 | a | 0.06706 | 0.11931 | 0.63075 | 1.0000 |
| S4 | S | 4 | a | 0.88315 | 0.19988 | 0.85682 | 1.0000 |
| S5 | S | 4 | a | 0.44132 | 0.20198 | 0.88688 | 1.0000 |
| S6 | S | 4 | a | 0.16916 | 0.47264 | 0.88203 | 1.0000 |
| S7 | S | 4 | a | 0.63154 | 0.44862 | 0.86479 | 1.0000 |
| S8 | S | 4 | a | 0.29364 | 0.37267 | 0.62282 | 1.0000 |



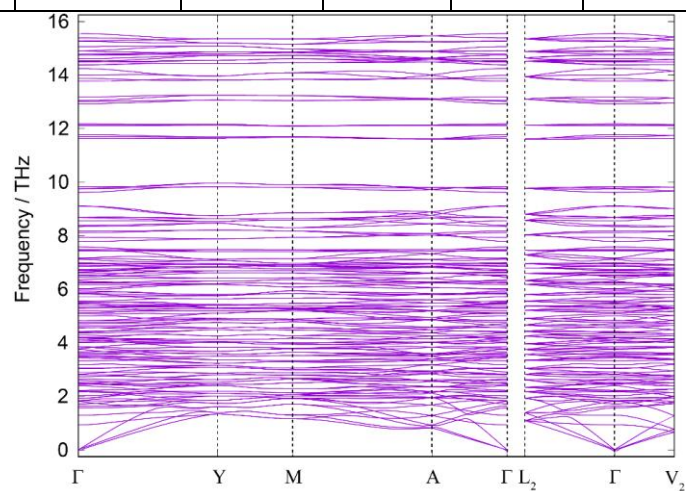**Figure S11.** *Calculated phonon dispersion curve of the newly found $Mg_3V_2S_8$ phase.*

**Table S5.** *Comparison of crystal structure parameters obtained from refinements of $Mg_3V_2S_8$ from PDF experiment and theoretically predicted structure.*

|  | VS$_4$ (PDF) | Mg$_3$V$_2$S$_8$ (calculated) | 1.1 V discharge_ B | 0.3 V discharge_ E | 1.8 V charge_ F |
|---|---|---|---|---|---|
| *a*/Å | 6.726 | 7.604 | 7.212 | 7.414 | 7.424 |
| *b*/Å | 10.466 | 13.350 | 13.650 | 13.740 | 13.766 |
| *c*/Å | 12.087 | 12.381 | 12.074 | 11.918 | 12.088 |
| β/° | 100.7 | 106.688° | 104.456 | 106.343 | 106.938 |
| Unit cell volume/ Å$^3$ | 836.06 | 1204.01 | 1150.97 | 1165.01 | 1181.788 |
| U$_V$ | 0.013 |  | 0.013 | 0.0149 | 0.0138 |
| U$_S$ | 0.013 |  | 0.012 | 0.0115 | 0.0128 |

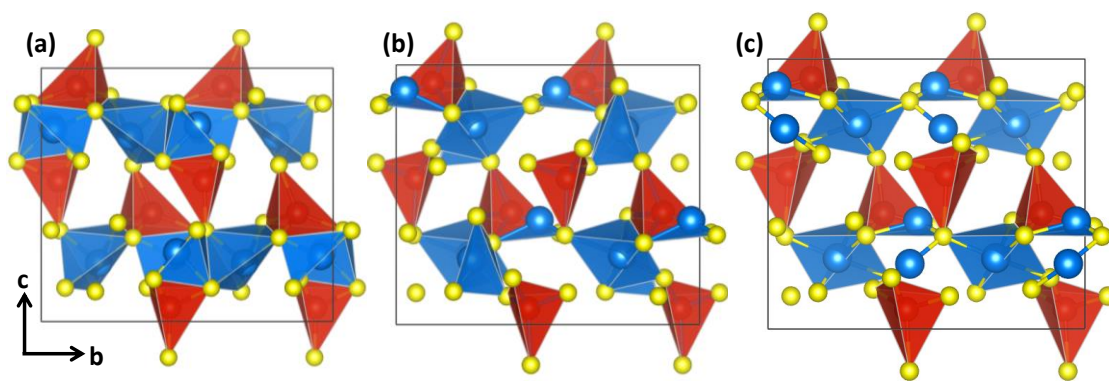**Figure S12.** *(a-c) The unit cell of* $Mg_3V_2S_8$ *for samples B, E and F as obtained* after subtracting the contribution of V metal from total PDF data. Mg, V and S atoms are represented by blue, red and yellow balls respectively.

## Section 4. Additional figures

**Table S5.** *DFT computed electrochemical potentials for various Mg conversion/insertion reactions involved. For insertion reactions, values for the most stable insertion product for each stoichiometry is shown.*

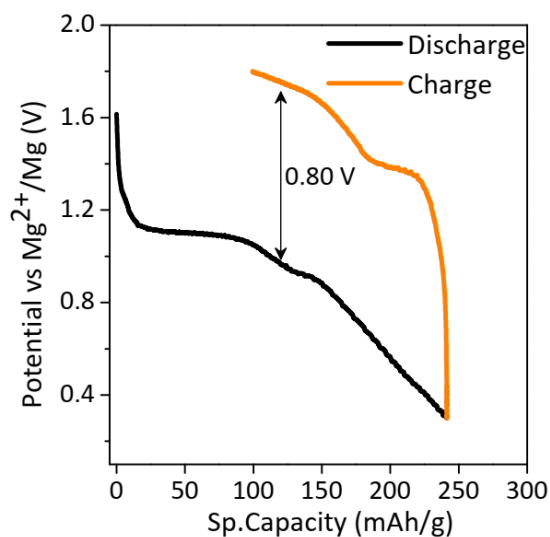| Reaction | DFT potential / V |
|---|---|
| $VS_4 + 1.5Mg \rightarrow 0.5Mg_3V_2S_8$ | 1.10 |
| $VS_4 + 4Mg \rightarrow V(fcc) + 4MgS$ | 1.04 |
| $VS_4 + 4Mg \rightarrow V(bcc) + 4MgS$ | 1.08 |



**Figure S13.** *Voltage- capacity curve of $VS_4$ cathode cycling against Mg anode at 293 K. The curve is for first cycle. The arrow marks the voltage hysteresis between discharge and charge.*
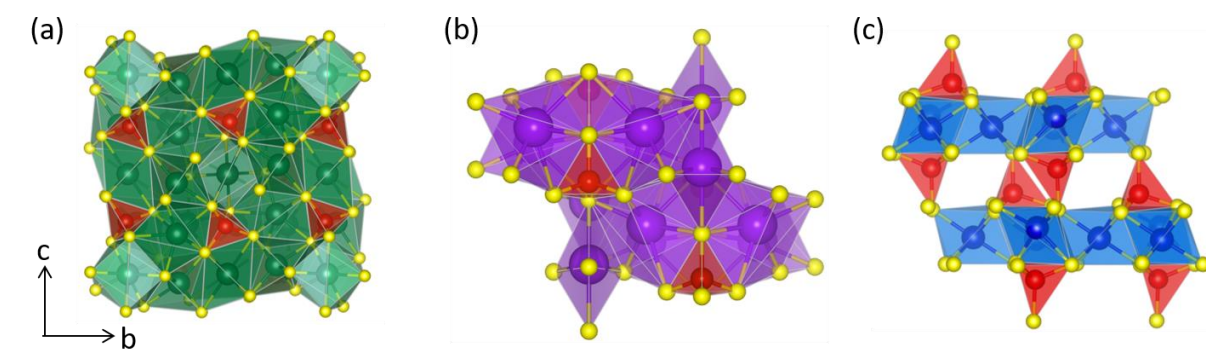
**Figure S14.** *Crystal structure of (a) Na₃VS₄ (space group P-421c, ICSD 84298), (b) K₃VS₄ (space group Pmcn, ICSD 74678)* [43, 44] *and (c) Mg₃V₂S₈. V and S atoms are marked by red and yellow colour respectively. Na, K and Mg atoms are indicated by green, violet and blue colour respectively. Na₃VS₄ crystallizes in tetragonal structure closely packed in all three directions where VS₄ T_d are separated by the NaS₆ Oh. K₃VS₄ crystallizes in orthorhombic structure consisting of VS₄ T_d separated by KS₇ and KS₅ units formed a close packed structure.*

**Table S6.** *Vanadium sulphur bond distances for different oxidation states of V and S. The data are obtained from CIF files of known structures.* BaVS3 (ICSD 86796), VS₂ (ICSD 68713), K₃VS₄ (ICSD 74678), VS₄ (ICSD 16797).

| Materials | V-S bond distances (Å) | V oxidation state | S oxidation state |
|-----------|------------------------|-------------------|-------------------|
| VS₂ | ~2.36 | +4 | -2 |
| BaVS₃ | ~2.37 | +4 | -2 |
| K₃VS₄ | ~2.15 (V-S1), ~2.163 (V-S2), ~2.147 (V-S3) | +5 | -2 |
| VS₄ | ~2.40 (reported+XPDF) | +4 | -1 |

**Table S7.** *DFT computed* $^{51}$*V NMR parameters of various vanadium sulphates considered in this study.*

| Materials | $\delta_{iso}^{calc}$ / ppm | $\delta_{iso}^{expt}$ / ppm | $\delta_{aniso}^{calc}$/ ppm | η | C_Q / MHz | η_Q |
|-----------|------|------|------|------|------|------|
| VS₄ | -164 | 163 | -568 | -0.1. | -1.84 | -0.2 |
| K₃VS₄ | 1229 | 1375 | 67 | 0.9 | 0.49 | 0.4 |
| Mg₃V₂S₈ | 1522 | 300-1300 | -221 | 0 | -0.67 | 0 |

**References.**

55.    A. Gupta, C. B. Mullins and J. B. Goodenough, *Electrochimica acta*, 2012, **78**, 430-433.

56.     S. Hayashi and K. Hayamizu, *Bulletin of the Chemical Society of Japan*, 1990, **63**, 961-963.
57.     B. Ravel and M. Newville, *Journal of Synchrotron Radiation*, 2005, **12**, 537-541.
58.     A. Hammersley, S. Svensson, M. Hanfland, A. Fitch and D. Hausermann, *Inter. J. of High Pressure Res.*, 1996, **14**, 235-248.
59.     X. Qiu, J. W. Thompson and S. J. Billinge, *Journal of Applied Crystallography*, 2004, **37**, 678-678.
60.     C. Farrow, P. Juhas, J. Liu, D. Bryndin, E. Božin, J. Bloch, T. Proffen and S. Billinge, *Journal of Physics: Condensed Matter*, 2007, **19**, 335219.
61.     V. Petkov, M. Gateshki, J. Choi, E. Gillan and Y. Ren, *J. Mater. Chem.* , 2005, **15**, 4654-4659.
62.     P. K. Allan, J. M. Griffin, A. Darwiche, O. J. Borkiewicz, K. M. Wiaderek, K. W. Chapman, A. J. Morris, P. J. Chupas, L. Monconduit and C. P. Grey, *J. Am. Chem. Soc.*, 2016, **138**, 2352-2365.
63.     J. P. Perdew, K. Burke and M. J. P. r. l. Ernzerhof, *Phys. Rev. Lett.* , 1996, **77**, 3865.
64.     G. Kresse and J. J. P. R. B. Hafner, *Phys. Rev. B* 1993, **47**, 558.
65.     A. Togo and I. Tanaka, *Scripta Materialia*, 2015, **108**, 1-5.
66.     S. J. Clark, M. D. Segall, C. J. Pickard, P. J. Hasnip, M. I. Probert, K. Refson and M. C. Payne, *Z. Kristallogr. Cryst. Mater.*, 2005, **220**, 567-570.